이학박사학위논문

First-principles study of non-collinear magnetic ordering and related properties in spinel Ir_2O_4 and delafossite $PdCrO_2$

제일원리 계산을 통한 spinel Ir_2O_4 와 delafossite $PdCrO_2$의 자기 구조 연구

2020년 2월

서울대학교 대학원
물리·천문학부
박 창 휘

First-principles study of non-collinear magnetic ordering and related properties in spinel Ir_2O_4 and delafossite $PdCrO_2$.

제일원리 계산을 통한 spinel Ir_2O_4 와 delafossite $PdCrO_2$의 자기 구조 연구.

지도교수 유 재 준

이 논문을 이학박사 학위논문으로 제출함

2020년 1월

서울대학교 대학원

물리·천문학부

박 창 휘

박창휘의 이학박사 학위논문을 인준함

2020년 1월

위 원 장 김 창영 (인)

부위원장 유 재 준 (인)

위 원 박 제근 (인)

위 원 민 홍기 (인)

위 원 한 명준 (인)

Abstract

First-principles study of non-collinear magnetic ordering and related properties in spinel Ir_2O_4 and delafossite $PdCrO_2$

Changhwi Park
Department of Physics and Astronomy
The Graduate School
Seoul National University

We study magnetic structures of delafossite $PdCrO_2$ and spinel Ir_2O_4. Delafossite $PdCrO_2$ is a layered triangular anti-ferromagnetic (AFM) system which consists of alternating Pd and CrO_2 layers. The metallic Pd layers contribute to high conductivity in *xy*-direction ,while local magnetic moments of Cr atoms contribute to anomalous Hall effect. From neutron diffraction and angle-resolved photoemission spectroscopy experiments, the magnetic structure of $PdCrO_2$ is expected to be triangular 120° AFM ordering in *xy*-plane and 6 layers structures in *z*-direction. However, the specific structures, such as scalar chirality, staggered chirality, twisted easy-planes, and easy-plane directions, are not clearly understood. Meanwhile, spinel Ir_2O_4 is a pyrochlore $J_{eff,1/2}$ system. The oxygen position and magnetic properties of Ir_2O_4 is not reported. Also, theoretical backgrounds of spinel $J_{eff,1/2}$ system is insufficient compared to pyrochlore 227 system, so there is only small information to study spinel Ir_2O_4. In this study, we calculate their magnetic structures and electronic structures

based on density functional theory (DFT). The ground structure of $PdCrO_2$ is the high-symmetric in-planar staggered chirality structure, and Ir_2O_4 is *mE* (local-*xy*) phase. We also suggest origins of magnetic structures, which are related to the nearest and 2nd nearest neighbor spin interaction models.

Keywords : Magnetism,Density functional theroy,Ir_2O_4,$PdCrO_2$

Student Number : 2013-20370

Contents

List of figures

Chapter 1

Introduction

The physical properties of magnetic materials are determined by the ground magnetic structure and excited states which are induced by external fields. However, magnetic properties of frustrated system are tends to be ambiguous because of their various possibilities of ground structure, excited states and interaction energy. Delafossite $PdCrO_2$ and spinel Ir_2O_4 are notable examples of it. The complexity of frustrated magnetic structure is always a huge obstacle to understand physical properties. However, it is also an origin of novelty of the system, we can find interesting phenomena by searching hidden magnetic structures. In this study, we concentrate on the specific magnetic structures of two materials. The two materials have not been fully understood from previous studies, they also have new possibility of novel physical properties.

First study is about delafossite $PdCrO_2$. Delafossite $PdCrO_2$ is a quasi two dimensional layered material which consists of CrO_2 insulating layers and Pd metallic layers. The bands near Fermi level are mostly occupied by Pd-*d* orbitals, but the local magnetic moments of Cr atoms play important role on both electronic bands and macroscopic quantities. Anomalous Hall effect (AHE) of $PdCrO_2$ is strongly related to the anti-ferromagnetic (AFM) structure of triangular Cr magnetic moments, so the analysis of the ground and excited magnetic structure is very important to understand AHE. For ten years, there have been numerous studies for $PdCrO_2$, including theoretical calculations. However, the experimental data, such as neutron scattering

and angle resolved photoemission spectroscopy (ARPES), still give us only limited information. It is because of their insufficient resolution and incomplete theoretical backgrounds. Among the possible candidates of the ground structure, we concentrate on the twisted two easy-planes model. From our calculation result, we expect that the result can be a new stepping point for the next progress of $PdCrO_2$ study.

Second study is about spinel Ir_2O_4, a pyrochlore $J_{eff,1/2}$ system. Pyrochlore system is famous for its potential of topological properties. One of the most intriguing properties of pyrochlores is that the topological phases are expected to be related to its magnetic phases. There have been numerous studies on 227 pyrhochlore systems. Even though the system does not have any topological properties, they still have novel magnetic structures because of its magnetic frustration. Unfortunately, there have been very few studies for spinel pyrochlores. Experimental data, theoretical approaches for the spinel system have just begun. We have very limited information on spinel Ir_2O_4; It is a spinel, pyrochlore structure, insulator with a small gap and Ir atoms have $J_{eff,1/2}$ orbitals, which is called spin-orbit Mott insulator. With recent studies on pyrochlore magnetic phases, such as m-order parameters, special properties on the m_E phase and Slater-Koster calculations, we predict the magnetic structure of spinel Ir_2O_4. We use density functional theory (DFT) calculations. Basically, DFT is a first-principle calculation, but it requires extra techniques to obtain better results for *d*-orbital non-collinear spin system. We added LDA+U and spin constraint methods. LDA+U is a typical method to compensate underestimate of Coulomb interaction of DFT. Also, spin constraint method is included to fix local spin directions at excited states. With the two empirical techniques, we successfully calculated magnetic structures in high precision. The high precision calculation is necessary for studying and predicting very precise magnetic structures, which have too small energy to be

found in contemporary experiments. We also combine model calculations. Among them, tight-binding method (TB) is the most practical method. It is a simplified calculation of DFT, but it gives intuitive idea for a good understanding. Consequently, we compare the DFT calculation with spin interaction models. The spin interaction model plus linear spin wave theory (LSWT) is the only theoretical method to analyse neutron scattering data. Therefore, connecting DFT data to a proper spin model is the most important process of a theoretical study.

Chapter 2

Computational methods

In this chapter, we introduce the basic theory and applications for calculating electronic and magnetic structures. We briefly introduce density functional theory and their practical application techniques for non-collinear spin calculations.

2.1 Density functional method

The density functional theory (DFT) is the most practical solution to calculate electronic and magnetic structures in condensed matter. Despite of its difficulty of interpretation for comprehensible models, DFT is the most powerful theoretical method because of its accuracy.

In this section, we introduce the basic concept and formula of DFT. First, we introduce the first idea by Hohenberg and Kohn [1]. Second, we introduce the concrete theorem Kohn-Sham approach, which is the basic idea to construct a practical density functional theory. Third, we introduce exchange-correlation functional. It generalize electron exchange-correlation energy with density functional.

2.1.1 Hohenberg-Kohn theorem

Hohenberg-Kohn theorem is the basic idea to establish the mathematical background of DFT theory.

Theorem 1. For any system of interacting particles in an external potential $V_{ext}(\mathbf{r})$, the potential $V_{ext}(\mathbf{r})$ is determined uniquely, up to addition by a constant,

by the ground state particle density $n_0(\mathbf{r})$.

Theorem 2. A universal functional for the energy $E[n]$ in terms of the density $n(\mathbf{r})$ can be defined, which is independent of the external potential $V_{ext}(\mathbf{r})$. For any particular $V_{ext}(\mathbf{r})$, the exact ground state energy of the system is the global minimum value of this functional, and the density $n(\mathbf{r})$ minimizing the functional is the exact ground state density $n_0(\mathbf{r})$.

Proof of theorem 1. The proof has a prerequisite of non-degenerated ground state. Suppose we have two external potentials $V_{ext,1}(\mathbf{r})$ and $V_{ext,2}(\mathbf{r})$, and corresponding Hamiltonian H_1 and H_2. Let the ground state of H_1 and H_2 are Ψ_1 and Ψ_2. If we assume densities of Ψ_1 and Ψ_2 are same $n_0(\mathbf{r})$, then

$$E_1 = \langle \Psi_1 | H_1 | \Psi_1 \rangle < \langle \Psi_2 | H_1 | \Psi_2 \rangle \tag{2.1}$$

$$\begin{aligned} \langle \Psi_2 | H_1 | \Psi_2 \rangle &= \langle \Psi_2 | H_2 | \Psi_2 \rangle + \langle \Psi_2 | H_1 - H_2 | \Psi_2 \rangle \\ &= E_2 + \int d\mathbf{r} \, [V_{ext,1}(\mathbf{r}) - V_{ext,2}(\mathbf{r})] n_0(\mathbf{r}) \end{aligned} \tag{2.2}$$

so that

$$E_1 < E_2 + \int d\mathbf{r} \, [V_{ext,1}(\mathbf{r}) - V_{ext,2}(\mathbf{r})] n_0(\mathbf{r}) \tag{2.3}$$

In the same way,

$$E_2 < E_1 + \int d\mathbf{r} \, [V_{ext,2}(\mathbf{r}) - V_{ext,1}(\mathbf{r})] n_0(\mathbf{r}) \tag{2.4}$$

By substituting two equations, we have

$$E_1 + E_2 < E_1 + E_2 \tag{2.5}$$

This contradiction arises from the assumption of the same density n_0.

Proof of theorem 2. If $n(\mathbf{r})$ is specified, the total energy function is determined by $n(\mathbf{r})$.

$$E_{HK}[n] = T[n] + E_{int}[n] + \int d\mathbf{r} V_{ext}(\mathbf{r}) n(\mathbf{r})$$
$$\equiv F_{HK}[n] + \int d\mathbf{r} V_{ext}(\mathbf{r}) n(\mathbf{r}) \tag{2.6}$$
$$\tag{2.7}$$

Since the ground state density $n_0(r)$ corresponds to external potential $V_{ext}(r)$, the ground energy of $V_{ext}(r)$ is

$$E_0 = E_{HK}[n_0] = \langle \Psi_0 | H_0 | \Psi_0 \rangle \tag{2.8}$$

and for a different density $n(r)$ which correspond to a different wave function Ψ

$$E_0 = \langle \Psi_0 | H_0 | \Psi_0 \rangle < \langle \Psi | H_0 | \Psi \rangle = E. \tag{2.9}$$

2.1.2 Kohn-Sham approach

Hohenberg-Kohn theorem guarantees the existence of energy functional based on density, but it does not give a practical method for real system. Kohn-Sham formula is the practical approach for it. Based on the density functional, Kohn-Sham formula replaces many-body interactions to an independent particles problem. The energy functional and Kohn-sham equation are as follows

$$
\begin{aligned}
E_{KS} &= T_s[n] + \int d\mathbf{r} V_{ext}(\mathbf{r}) n(\mathbf{r}) + E_{Hartree}[n] + E_{II} + E_{xc}[n], \\
T_s[n] &= \frac{1}{2} \sum_{i=1}^{N} |\nabla \psi_i|^2, \\
E_{Hartree}[n] &= \frac{1}{2} \int d\mathbf{r} d\mathbf{r}' \frac{n(\mathbf{r}) n(\mathbf{r}')}{|\mathbf{r} - \mathbf{r}'|}
\end{aligned} \tag{2.10}
$$

and the Kohn-Sham equation is

$$
\begin{aligned}
[-\frac{\hbar^2}{2m} + V_{KS}(r)]\Psi_i(r) &= \varepsilon_i \Psi_i(r), \\
V_{KS}(r) &= V_{ext}(r) + V_{Hartree}(r) + V_{XC}(r), \\
V_{Hartree}(r) &= \int dr' \frac{n(r')}{|r - r'|}, \\
V_{XC}(r) &= \frac{\delta E_{XC}[n(r)]}{\delta n(r)}
\end{aligned} \tag{2.11}
$$

The solution of the equation generates the density

$$
n(r) = \sum_{i=1}^{N} |\Psi_i(r)|^2 \tag{2.12}
$$

The minimization of energy with density $n(r)$ give the solution of Kohn-Sham equation, and it can be obtained by iterative solving of independent eigen functions and the density $n(r)$. However, the exchange-correlation functional E_{xc} is a subtle point. A proper choice of exchange-correlation functional is the essence of Kohn-Sham approach.

2.1.3 Exchange-correlation functional

A perfect exchange-correlation functional to solve Kohn-Sham equation is still unknown. In this section, we introduce two major exchange-correlation functionals, which are widely used in DFT packages. They are local density approximation (LDA) functional and generalized gradient approximation (GGA) functional.

The LDA method assumes that the exchange-correlation function is local. The basic LDA form is

$$E_{xc}^{LDA}[n] = \int d\mathbf{r} n(\mathbf{r}) \varepsilon_{xc}^{LDA}(n(\mathbf{r})) \tag{2.13}$$

The local density functional $\varepsilon_{xc}^{LDA}(n(r))$ is decomposed into exchange and correlation terms

$$\varepsilon_{xc}^{LDA}(n(\mathbf{r})) = \varepsilon_{x}^{LDA}(n(\mathbf{r})) + \varepsilon_{c}^{LDA}(n(\mathbf{r})) \tag{2.14}$$

The first idea to construct exchange-correlation functional starts from homogeneous electron gas. With the assumption of homogeneous electron and quantum Monte Carlo calculation, optimized LDA coefficients was reported as follows [2].

$$\varepsilon_{x}^{LDA}(n(r)) = -\frac{3}{4}\left(\frac{3}{\pi}\right)^{1/3} \tag{2.15}$$

and

$$\varepsilon_c^{LDA}(n(r)) = \begin{cases} Alnr_s + B + Cr_s lnr_s + Dr_s, & if \quad r_s \leq 1 \\ \gamma/(1+\beta_1\sqrt{r_s}+\beta_2 r_s), & if \quad r_s > 1 \end{cases}$$

$$r_s = (3/4\pi n)^{1/3} \tag{2.16}$$

The optimized coefficients by Perdew and Zunger are $A = 0.0311, B = -0.048, C = 0.002, D = -0.0116, \gamma = -0.1423, \beta_1 = 1.0529, \beta_2 = 0.3334$ (Hartree unit).

Meanwhile, GGA functional is a modification of LDA by expanding gradient of density ∇n. A generalized form is as follow

$$E_{xc}^{GGA}[n] = \int drn(r)\varepsilon_{xc}(n, |\nabla n|, ...). \tag{2.17}$$

Among GGA functionals, the GGA-PBE functional, which is proposed by Perdew, Burke and Enzerhof [3] is widely used.

2.1.4 Pseudopotential

Because of the atomic potential near nuclei, the potential energy in condensed material has sharp peaks. The infinite-peak makes the numerical calculation extremely hard, especially for plane-wave basis set. The pseudopotential method is an idea to avoid that problem [4]. It replaces the strong Coulomb peak at nucleus position to an effective potential. The potential is a screened potential by core electrons, it can be used as an effective potential for valence electrons while core electrons are frozen. When atomic orbital basis set is used, the atomic basis set must be corrected to corresponding pseudo atomic orbitals. There is not a specific form of pseudopotential, because pseudopotentials can be modified by its core electron numbers, calculation

efficiency and accuracy (e.g. cut-off radius and ultrasoft pseudopotential). The following form is the general description of pseudopotential

$$\hat{V}_{PS}(r) = \sum_{l=0}^{\infty} \sum_{m=-l}^{l} v_{PS}^{l}(r) \left|lm\right\rangle \left\langle lm\right| \tag{2.18}$$

Generally, pseudopotential has projection terms corresponding to angular momentum.

Details of pseudopotential can be also modified along with exchange-correlation terms, non-collinear spin description and the number of core electrons. Therefore, a proper selection of pseudopotential in accordance with calculation purpose is important.

2.2 Application of DFT method

The DFT calculation method is one of the most successful achievements in condensed matter physics. However, they still have many flaws, since the density functional exchange-correlation term itself is the intrinsic problem of DFT. There have been numerous efforts to correct drawbacks with the first-principle method. However, the correction with empirical parameters often gives better solutions.

In this chapter, we introduce practical applications to calculate non-collinear spin in d orbital system. First, we introduce how different orbital basis and plane-wave basis methods are. Second, we introduce LDA+U method. It easily corrects the underestimated Coulomb interaction energy in DFT. Third, we introduce spin constraint method. It helps to fix the magnetic structure as we intended. By combining empirical methods, we successfully calculated non-collinear spins of d orbital electrons. For better quality of high precision DFT calculations, additional setting details

are also required in each DFT code.

2.2.1 Atomic orbital basis set

Plane-wave basis set and atomic orbital basis set are the two wave function methods which are widely used in DFT calculation. Plane-wave basis is the most common basis set of DFT calculation. It has advantage on completeness of basis, since the plane-wave set becomes the complete set when cut-off energy (k^2) is expanded to infinite. Although the infinite cut-off energy is practically impossible, at least, the plane-wave basis is getting close to the complete set when the cut-off energy increases. Plane-wave also has benefits on reciprocal lattice calculations like band-unfolding method.

Meanwhile, atomic orbital basis [5] gives more intuitive information to study atom and orbital properties. To construct localized magnetic moments, atomic charge and Hubbard interaction U, plane-wave basis function requires additional projection orbitals, which can cause an inefficiency. However, atomic orbital basis set is free from that problem, since it has atomic orbitals intrinsically. One problem of atomic orbital basis is that it does not guarantee the completeness of basis even though the number of atomic orbital basis increases to infinite. Also, atomic orbital basis set has a disadvantage on reciprocal lattice calculations like band-unfolding [6]. Nevertheless, the advantage of atomic orbital basis set outweigh its disadvantage in non-collinear spin calculations. Therefore, for efficiency of calculation, we use a orbital basis DFT code OpenMX for the main DFT calculation method. For the complementary cross-checking, we use plane-wave basis code VASP. The two codes generally give similar results but only small difference in energy scale, magnetic moments and charge occupation numbers, which are originated from projection orbital difference.

Coulomb interaction term U should be carefully used for two different codes,

since they have different projection orbitals for U. The relation between U and gap size or band dispersion of two codes has to be checked before main calculations, especially for small gap systems.

2.2.2 LDA+U method

Density functional method with LDA or GGA exchange-correlation functional tends to underestimate local Coulomb interactions. In the most of cases, electrons in d and f orbitals require additional local Coulomb interaction energy. However, the extra Coulomb energy for correct calculation is not well defined. From experimental data and many DFT calculations with different settings, we emprically estimate Coulomb interaction energy for each atom. LDA+U total energy funtional is simply defined by [7]

$$
\begin{aligned}
&E_{LDA+U} = E_{LDA} + E_U, \\
&E_U = \frac{1}{2}\sum_{\alpha} U_\alpha \sum_{\sigma,m,m'} n^{\sigma}_{\alpha m} n^{-\sigma}_{\alpha m'} + \frac{1}{2}\sum_{\alpha} (U_\alpha - J_\alpha) \sum_{\sigma,m\neq m'} n^{\sigma}_{\alpha m} n^{\sigma}_{\alpha m'}
\end{aligned}
\tag{2.19}
$$

where α is atomic orbital index, m labels are localized states of same atomic orbital site and σ is spin index. In practical DFT packages, atomic orbital basis tools like OpenMX easily define Coulomb interaction orbitals. However, plane-wave basis tools like VASP does not have orbital definition, so they have to define projection orbital for Coulomb interaction. It makes energy difference between orbital basis and plane-wave basis tools. Because of that, we need extra efforts to adjust U for each DFT package.

2.2.3 Spin constraint method

To find the ground magnetic structure, we have to find the ground energy of the system. However, we also have to calculate excited states to find various kinds of magnetic structures and their spin interaction energies. One problem of it is that DFT calculation is a method for ground state finding, basically. It does not calculate excited states unless the calculation is trapped in a local minimum state. Therefore, to make excited magnetic structures and local spin directions as we intended, there must be extra spin constraint methods.

Penalty function constraint is a widely used method for it. This method gives penalty energy when selected spins are rotated from the intended spin direction. As a result, the intended magnetic structure becomes the ground state if the penalty energy is strong enough. If the energy of target magnetic structure is much larger than energy of ground state, it would require a very strong penalty function energy. However, the strong penalty function easily makes SCF to diverge. Therefore, although the penalty function method is a good calculation scheme for the most of non-collinear spin system, it is not suitable for the excited state calculation of strong spin interaction system.

Zeeman constraint method is also a good approach. This method gives additional Zeeman interaction energy on local magnetic moments, induces each spin to converge to the intended direction. The Zemman constraint method is relatively free from SCF diverging problems, so very strong Zeeman constraint can be applied to spins. However, the strong Zeeman interaction energy induces a stretching effect on spins, enhances magnetic moments. Therefore, when Zeeman constraint is adopted for the sake of strong constraint, there must be additional energy corrections to compensate the spin stretching effect.

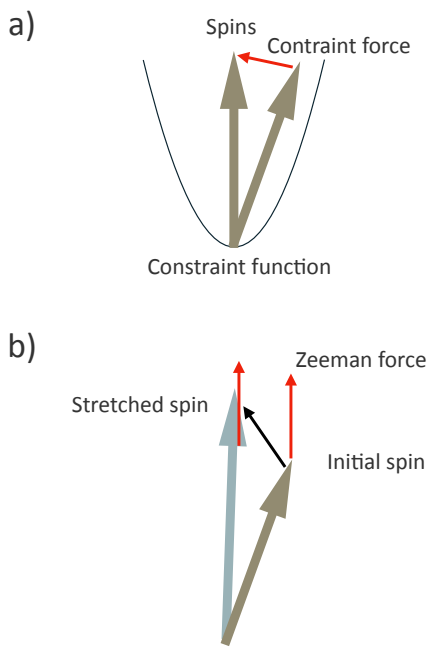

Fig. 2.1: Schematic figures of two constraint methods. a) Penalty function method. The penalty function gives extra energy when the local spin is rotated from intended spin direction. b) Zeeman constraint method. The force by local Zeeman interaction energy induces the spin to intended direction. The Zeeman constraint is suitable when the strong constraint is required. However, it gives a stretching effect of spin, leads to extra energy from stretched spins. The energy from stretching effect must be corrected.

2.2.4 Practical applications for non-collinear spin calculation

The combination of LDA+U and spin constraint method is widely used in magnetic structure calculations. For easy magnetic systems, the combination method is good enough. However, if the target system requires very strong constraint, high precision and low SCF-criterion, extra DFT settings should be added for the correct calculation.

Strong spin constraint energy generally makes extra errors. To reduce the error, small constraint energy is necessary, but the problem is when magnetic excited energy is large. In this case, instead using a strong constraint, it is recommended to make other DFT setting to focus on convergence. First, the initial spin directions for target structures have to be set very specifically. Because without user guide, the DFT setting focused on convergence hardly find the ground state. Second, in OpenMX, RMM-DIISH is a good mixing scheme for non-collinear spin calculations. It is a Hamiltonian mixing scheme, and known to be effective for the non-collinear spin calculation. RMM-DIISH has a weak point on metallic system, since the mixing tends to make charge sloshing effect, disturbing SCF convergence. However, it has tendency of local minimum convergence, so it can be a good choice for non-collinear excited state calculations. Meanwhile, VASP has its optimized hybrid mixing scheme. VASP tends to converge at local minimum state more easily than OpenMX, so the VASP-optimized mixing algorithm is good enough for non-collinear calculations. However, the easy converging is not always a better option for non-collinear calculations. Because that means that the DFT hardly finds the ground state. Third, there is a difference in LDA and GGA. Both of them are reliable for the spin constraint calculation, and they generally give similar results. However, GGA methods tend to require more Ngrids than LDA to get similar level of error. Therefore, to reduce errors of non-collinear directions and energies, LDA functional can be a better choice.

In spite of this efforts, the spin constraint method is still the most important factor. Penalty function energy and Zeeman interaction energy can be easily subtracted from total energy. The difficult problem is the energy from stretched spins, since each system has its different response energy to stretched spins. To correct it, we have to check the energy response to the stretched spins. By changing Zeeman interaction energy, we can intentionally stretch magnetic moments from ground state moments. In this cases, total energy of the system generally has quadratic curves to stretched magnetic moments, so we can fit the energy curve to it. Then, with the quadratic fitting function, we can generate error correction functions. This correction method becomes important when we need strong constraints. In practical calculations, we used the correction method for Ir_2O_4 m-order parameters calculations.

2.3 Tight-binding method

Although DFT calculations gives the most refined theoretical result of the solid state system, the output of DFT calculation is very hard to understand. What we easily understand is only the final results such as energy, ground state and some excited states. For a simple explanation, we need a simple description for the electronic structure. The best solution of it is the tight-binding (TB) method.

Compared to DFT calculations, TB method is just a simplified form of electronic interactions. Basically, the TB method regards a system as sum of electronic hoppings. For example, if the TB description is maximally simplified, the TB Hamiltonian can be written as

$$\hat{H} = \sum_{i,j} t_{ij} c^{\dagger}_{i\sigma} c_{j\sigma'} \tag{2.20}$$

where σ is spin index, i and j are indices for hopping sites, $c^{\dagger}$ (or c) is creation (or annihilation) operator and t_{ij} is a constant. We can define various kinds of interactions by giving restrictions on hopping sites and hopping constant t, but the Hamiltonian must be a Hermitian form.

To solve the general TB form, we construct a matrix description of Hamiltonian in the reciprocal space. Let's assume the basis in real space $\varphi(\mathbf{r})$. Then, the basis function in Bloch form is

$$\phi_{\alpha\mathbf{k}}(\mathbf{r}) = \frac{1}{\sqrt{N}} \sum_{\mathbf{R}} e^{ik\cdot(\mathbf{R}+\tau_\alpha)} \varphi_\alpha(\mathbf{r}-\mathbf{R}-\tau_\alpha) \tag{2.21}$$

where α is orbital index in sublattice, τ_α is the position in sublattice and $\mathbf{R}$ is lattice position in N cells. We can derive the eigenvalue and eigenstate of TB Hamiltonian in the following form

$$H\Psi_{nk} = E_{nk}\Psi_{nk}. \tag{2.22}$$

Let's assume the Hamiltonian is

$$\begin{aligned} H &= \frac{p^2}{2m} + V(\mathbf{r}) + \sum_{\mathbf{R}\neq 0} V(\mathbf{r}-\mathbf{R}) \\ &= H_{atom} + \Delta V, \end{aligned} \tag{2.23}$$

and assume the eigenstate is

$$\Psi_{nk}(\mathbf{r}) = \sum_{\alpha} c_{\alpha nk}\phi_{\alpha k}(\mathbf{r}). \tag{2.24}$$

Then, the eigenvalue problem is

$$\sum_{\beta} H_{\alpha\beta}(\mathbf{k}) c_{\beta nk} = E_{nk} \sum_{\beta} S_{\alpha\beta}(\mathbf{k}) c_{\beta nk}, \tag{2.25}$$

where

$$\begin{aligned} H_{\alpha\beta}(\mathbf{k}) &= \left\langle \phi_{\alpha k} | H | \phi_{\beta k} \right\rangle \\ &= \sum_{\mathbf{R}} \int \mathbf{dr} e^{i\mathbf{k}\cdot(\mathbf{R}+\tau_\beta-\tau_\alpha)} \varphi_\alpha^*(\mathbf{r}-\tau_\alpha) H \varphi_\beta(\mathbf{r}-\mathbf{R}-\tau_\beta) \\ &= \sum_{\mathbf{R}} e^{i\mathbf{k}\cdot(\mathbf{R}+\tau_\beta-\tau_\alpha)} (\varepsilon_\alpha s_{\alpha\beta}(\mathbf{R}) + h_{\alpha\beta}(\mathbf{R})) \end{aligned} \tag{2.26}$$

and

$$S_{\alpha\beta}(\mathbf{k}) = \left\langle \phi_{\alpha k} | \phi_{\beta k} \right\rangle = \sum_{\mathbf{R}} e^{i\mathbf{k}\cdot(\mathbf{R}+\tau_\beta-\tau_\alpha)} s_{\alpha\beta}(\mathbf{R}) \tag{2.27}$$

with

$$s_{\alpha\beta}(\mathbf{R}) = \int \mathbf{dr} e^{i\mathbf{k}\cdot(\mathbf{R}+\tau_\beta-\tau_\alpha)} \varphi_\alpha^*(\mathbf{r}-\tau_\alpha) H_{atom} \varphi_\beta(\mathbf{r}-\mathbf{R}-\tau_\beta), \tag{2.28}$$

$$h_{\alpha\beta}(\mathbf{R}) = \int \mathbf{dr} e^{i\mathbf{k}\cdot(\mathbf{R}+\tau_\beta-\tau_\alpha)} \varphi_\alpha^*(\mathbf{r}-\tau_\alpha) \Delta V \varphi_\beta(\mathbf{r}-\mathbf{R}-\tau_\beta). \tag{2.29}$$

Finally, the general form of the eigenvalue problem is

$$\sum_{\beta} \left[H_{\alpha\beta}(\mathbf{k}) - E_{nk} S_{\alpha\beta}(\mathbf{k}) \right] c_{\beta nk} = 0. \tag{2.30}$$

$h(\mathbf{R})$ corresponds to hopping term, and $S(\mathbf{k})$ becomes an identity matrix when we assume orthogonal orbital basis.

However, in the most cases of d-electron systems, they require local Coulomb

interaction terms. In this case, TB model should be corrected to Hubbard model. The simplest form of Hubbard model is

$$\hat{H} = t \sum_{i,j,\sigma} (\hat{c}^{\dagger}_{i\sigma} \hat{c}_{j\sigma} + \hat{c}^{\dagger}_{j\sigma} \hat{c}_{i\sigma}) + U \sum_{i=1}^{N} \hat{n}_{i\uparrow} \hat{n}_{i\downarrow} \tag{2.31}$$

where $\hat{n}_{i\sigma}$ is occupation number operator on i, σ. Generally, Hubbard model is not solvable in an exact form. The only practical solution of it is mean-field approximation. With a given U, the electronic structure of Hubbard model can be solved iteratively and numerically. The mean-field approximation of Hubbard interaction term is achieved by

$$U \sum_{i=1}^{N} (\hat{n}_{i\uparrow} \langle \hat{n}_{i\downarrow} \rangle + \langle \hat{n}_{i\uparrow} \rangle \hat{n}_{i\downarrow} - \langle \hat{n}_{i\uparrow} \rangle \langle \hat{n}_{i\downarrow} \rangle). \tag{2.32}$$

One problem of the iterative mean-field calculation method is local-minimum trapping problem. As many other numerical optimization methods, it is often trapped in local minimum states. They sometimes change the magnetic moment of local spins, which is far from the experiments and DFT expectation. Therefore, a proper supervision of user is necessary. If the Hubbard model calculaton is conducted with non-collinear spin, initial spin directions and moments are very important.

TB and Hubbard model calculations are rough calculation methods, but they are still powerful and widely used approach in material physics because of its computational efficiency.

2.4 Effective spin model

Neutron scattering experiment is the most powerful method to analyse magnetic structures of condensed matter. Neutron diffraction gives the information of magnetic ground state, while neutron inelastic scattering gives energy and momentum information of excited states. To analyse the magnetic structure from neutron data, there must be theoretical backgrounds to connect the data to comprehensible magnetic structures. Linear spin wave theory (LSWT) is a practical method of it. LSWT provide a proper function to connect the neutron inelastic scattering to a correlation function of spins in the material.

The spin-spin interaction energy is a hypothetical concept. In the condensed material, electronic wave functions are spread in vicinity of atoms. The sum of spread electron spins near an atom can be considered as an fictitious local magnetic moment. When the magnetic structure changes, it is actually a change of electronic structure. Therefore, the energy of magnetic structure is a hypothetical concept by simplifying electronic energy. Nevertheless, the concept of spin interaction energy is a powerful approach to analyse magnetic structures. Among the various kinds of spin interaction functions, spin-spin interaction is the only practical method so far, since the LSWT uses that form only. It is a two spin interaction form, which can be written by

$$H = \sum_{i,j} J_{ij}^{\alpha\beta} S_i^{\alpha} S_j^{\beta}, \tag{2.33}$$

where S is a non-collinear spin in 3-dimensional space, J is a matrix of interaction energy, i and j are atomic position index, and α and β are directional index of non-collinear spin in (x, y, z). By giving proper restrictions, it can make various kinds of interaction energy such as Heisenberg interaction and Dzyaloshinskii-Moriya interac-

tion. By searching the ground magnetic structure, interaction energies and simulating LSWT, we can compare the simulated magnetic structure to neutron scattering data. One problem of the LSWT method is that we cannot calculate multi-spin interaction models such as four spins and six spins interaction models, since the LSWT is based on the two spin interaction model.

The spin interaction model is not automatically obtained from DFT calculation. We have to extract the interaction terms from DFT data fittings. With candidates of possible spin interaction models, a series of magnetic structure sets should be calculated. Correct energy calculations of excited magnetic structures are essential, including the ground state. It is hard process because the excited state in DFT always creates errors, and many of excited states fail to converge. To avoid over-fitting problem in spin interaction model, the number of well-converged magnetic structures has to outnumber the degree-of-freedom of interaction models. Also, SCF-convergence is very important. SCF-criterion in non-collinear calculation have to be much lower than normal DFT calculations, because spin interaction energy is very low in general. To achieve these goals, very careful DFT calculation setting and numerous trial-and-errors are required.

2.5 Summary of computational methods

We introduced a key concept of theoretical analysis of non-collinear magnetic structures. We use DFT with empirical parameter methods such as LDA+U and spin constraint methods. We use TB and effective spin interaction models consequently, they give comprehensible intuitions. With the calculation methods, we study delafossite $PdCrO_2$ and spinel Ir_2O_4 in the next two chapters. $PdCrO_2$ has very small magnetic structure energies, so we do not need strong spin constraint for it. Instead, lower-

ing the SCF-criterion is very important for this system. Meanwhile Ir_2O_4 has strong magnetic interaction energies, so it require strong spin constraint function for excited states. In this case, the energy correction method is important to compensate the error from spin constraint method.

Chapter 3

Delafossite $PdCrO_2$

The metallic delafossite $PdCrO_2$ is known to be a two-dimensional triangular Heisenberg anti-ferromagnet [8–16] with $T_N = 37.5K$. It has alternating layers of Pd and CrO_2 triangular lattices, respectively. The triangular lattice of Pd atoms construct metallic layers, responsible for the high conductivity within the layer along the *xy*-directions, while the CrO_2 layers are expected to be insulating layers with the local magnetic moments of Cr^{3+}(*S*=3/2). The reported a neutron diffraction peaks at $hkl = (1/3, 1/3, n/2)$ [8], indicate that $PdCrO_2$ has $\sqrt{3} \times \sqrt{3} \times 2$ supercell magnetic structure (e.g., AFM structure of three Cr atoms and 6-layer structure in *z*-direction). This magnetic supercell with the 120°-ordering of three Cr local moments is consistent with Yamaji angles [17], quantum oscillations [10] and a direct observation by angle resolved photoemission spectroscopy (ARPES).

Although the 120° magnetic ordering of Cr^{3+}(*S*=3/2) moments is expected to be the basic structure, there are still a lot of controversies on its details. Takatsu and coworkers [11] suggested a series of non-collinear 6-layer magnetic structures. Some of them are based on the previous study of $LiCrO_2$ [18], but others have more complicated details. A spin scalar chirality model, which contains non-coplanar spin ordering, was suggested as a possible candidate. However, it is still under controversy, since a direct evidence of scalar chirality is not observed also scalar chirality is not the only origin of anomalous Hall effect [19, 20]. Among the Takatsu's 6-layer in-planar models, a staggered chirality model is a strong candidate. The chirality of

three in-planar local magnetic moments can be defined by their rotation direction. In the system with three in-planar spin moments with 120° AFM ordering, there are only two rotation directions, i.e, handedness or chirality. The chirality can be defined by its stacking ordering of assigned atom indices and the rotation direction of spins of them. Depending on the stacking sequence of chiralities, the system can have multi-layer periodicity along the z-axis. Indeed, Manh Duc Le and coworkers [14] suggested a simpler model, a staggered chirality with 2 layers. Not only the 2-layer model reduces the number of model parameters, it also gives a better fitting quality for neutron inelastic scatterings and linear spin wave theory [21]. By employing the linear spin wave theory with seven fitting parameters, they have successfully suggested a Heisenberg model. However, although their interpretation describes well neutron inelastic scattering data, that model still have a limitation. The Heisenberg interaction only does not distinguish the energies of staggered and straight chiralities. Also, there is another remaining issue related to the easy-plane and local-easy-axis directions. The easy-plane and easy-axis direction of the ground-state magnetic configuration is still ambiguous. Further, there is no apparent clue for easy-plane and local-easy-axis problems.

The Fermi surface of $PdCrO_2$ has a nearly hexagonal shape [12]. Similar structures of ABO_2 delafossite, which have Pd or Pt atoms on A-site also have hexagonal shapes of Fermi surfaces [22], yet $PtCoO_2$ has a concave shape compared to $PdCoO_2$ [23, 24]. The xy-planar resistivity of $PdCrO_2$ at room temperature (295K) was found to be very low, $\approx 9\mu\Omega$ cm, while z-directional resistivity is high ($\rho_c/\rho_{ab} \geq 150$) [25, 26]. In contrast with $PdCoO_2$, which does not have magnetic moments on B-site, intriguing features of $PdCrO_2$ is its band folding, magnetic ordering and unconventional anomalous Hall effect [9]. There is also an issue on folded Fermi surface. The

spectral weight of folded Fermi surface is very weak, so there should be an explanation for it. A recent theoretical study suggested that the band folding effect of $PdCrO_2$ is originated from Kondo lattice Hamiltonian [27]. They explained weakened spectral weight of folded bands is caused by strong Coulomb repulsion U on Cr atoms.

Here, we investigate electronic and magnetic structures of $PdCrO_2$ by carrying out non-collinear spin density-functional-theory calculations. We also set up a tight-binding Hamiltonian to describe electronic bands and the Fermi surface which are correlated to magnetic structures. We suggest an effective spin model for the observed and calculated magnetic structure. We also demonstrate that the magnetic structures of Cr atoms affect both the z-directional electron hopping and the tiny degeneracy breaking on Pd bands.

3.1 methods

We carried out non-collinear spin DFT calculations to determine a series of magnetic orderings and their corresponding total energies. We used the OpenMX code [5, 28, 29]. $\sqrt{3} \times \sqrt{3} \times 2$ supercell was used to describe magnetic structures (Fig. 3.2). Minimum $32 \times 32 \times 90$ Ngrids and $10 \times 10 \times 10$ Kpoints grids are used for fast calculations. Maximum $64 \times 64 \times 180$ Ngrids and $14 \times 14 \times 14$ Kpoints are used for the convergence checking. We used $s^2p^2d^2f^1$ pseudo-atomic orbitals for Pd and Cr atoms, and $s^2p^2d^1$ for O atoms. SCF-criterion of 4×10^{-8} Hartree / 6-Cr atoms is used to guarantee the energy convergence for the spin configuration of easy-plane and local-axis rotation modes (approximately 10μeV / 1-Cr atom). A penalty-function-constraint method [30] and a Zeeman spin constraint method were used to constraint the non-collinear spin configurations. Although the penalty-function spin constraint can cause small error of spin directions, the error can be less than 0.1% from the

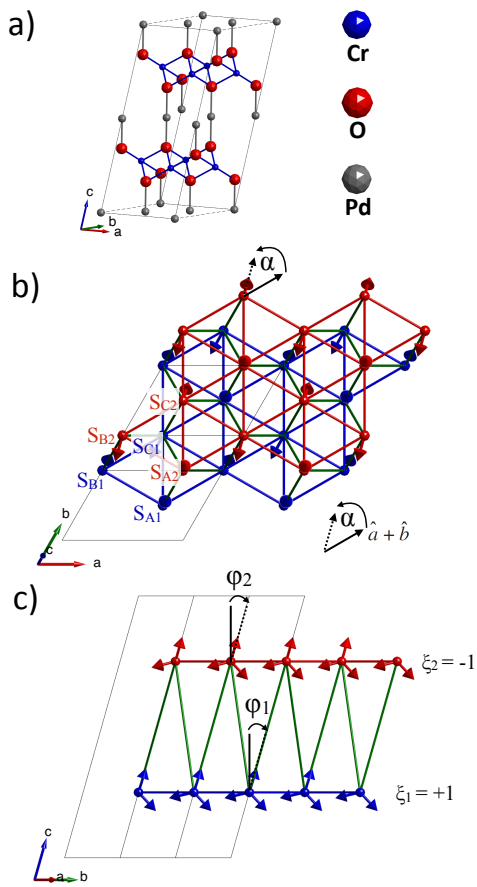

Fig. 3.2: Unit cell and a magnetic structure of $PdCrO_2$. a) The 2-layers cell with 3-Cr atoms in one layer is the smallest unit cell to represent a staggered chirality. b),c) An example magnetic structure of $\alpha_1 = 31$, $\alpha_2 = 44$, $\phi_1 = 17$, $\phi_2 = 16$, $\xi_1 = +1$, $\xi_2 = -1$. The 1st layer is painted blue, 2nd layer is painted red. Arrows indicate spin moments of Cr^{3+}. 1st nearest inter layer interactions are colored in green. 2 layers have their easy-planes (α) and easy-axes (ϕ) independently, which are illustrated in Eq. (3.1). When $\alpha = 30°, 150°, 270°$, the spin easy-planes align to the direction of 1st nearest inter layer interaction connections.

intended spin direction. We used RMM-DIISH [31] mixing scheme within the local spin density functional of Ceperley-Alder (LSDA-CA) [2] The RMM-DIISH is a suitable mixing scheme for non-collinear spin calculations. In non-collinear spin calculation, LSDA-CA tends to require less Kpoints than generalized gradient approximation (GGA) to reduce the error in determining spin directions. We used a combination of RMM-DIISH mixing and LSDA-CA functional for the better efficiency. To describe the on-site Coulomb interaction for Cr atoms, we used the LDA+U method [32]. Effective U=3.7eV was adopted for Cr d orbitals. The value is taken from previous $LiCrO_2$ study [33] and the material project data [34].

3.2 Results

3.2.1 Optimized crystal structure

First, we optimize the unit cell with OpenMX package. Starting from the experimental cell parameters $a = 2.923\mathring{A}$, $c = 18.08\mathring{A}$ and internal coordinate $z = 0.1105$ described in [14], we obtained the DFT-optimized cell parameters: $a = 2.889\mathring{A}$, $c = 17.867\mathring{A}$ and $z = 0.1099$. The slightly underestimated cell volume is known to be

Table. 3.1: Total energies for different magnetic configurations. The 120° AFM with staggerd chirality structure is determined to be the ground state, while the configuration with a straight chirality has 0.22 meV larger energy. Other collinear models have much higher energies regardless their direction or multi-layer ordering structures.

	meV/Cr atom
AFM staggered chirality	0.00
AFM xy easy plane, staggered chirality	0.014
AFM straight chirality	0.22
AFM xy easy plane, straight chirality	0.23
AFM collinear	27.88
FM collinear	27.06

a typical case expected from the use of the LDA exchange-correlation functional, whereas the agreement of the internal coordinate z is remarkable. Fig. 3.2 illustrates the triclinic unit cell which we choose for our DFT calculations. The conventional hexgonal unit cell requires 6 layers to describe even number periodicity like staggered chirality. The 6-layer supercell has an advantage for describing various kinds of 6-layer structures, but the inefficiency of a larger cell size makes the high precision calculations difficult practically. Therefore, we adopted a minimal cell, which can describe the directional degree of freedom for all Cr local magnetic moments with the layer and the even number periodicity along the z-direction.

Given the optimized unit cell, we calculate total energies for all the relevant spin configurations and analyze them by introducing effective spin models. We also present Fermi surfaces, which is dependent on the magnetic ordering. To describe the $k_z = 0$ plane, we use b_1 and $b_2 + \frac{2}{3}b_3$ vectors, instead the reciprocal vectors b_1 and b_2, because the reciprocal lattice vectors of the triclinic unit cell do not have C_3 symmetry.

3.2.2 Magnetic structures

As shown in Table 3.1, the ground-state magnetci configuration has a 120° AFM ordering in the layer, staggered chirality structure along z-direction and high symmetric co-planar easy-planes and local-easy-axis (Fig. 3.8). The ground magnetic structure can be described by the expression suggested in Ref. [11]:

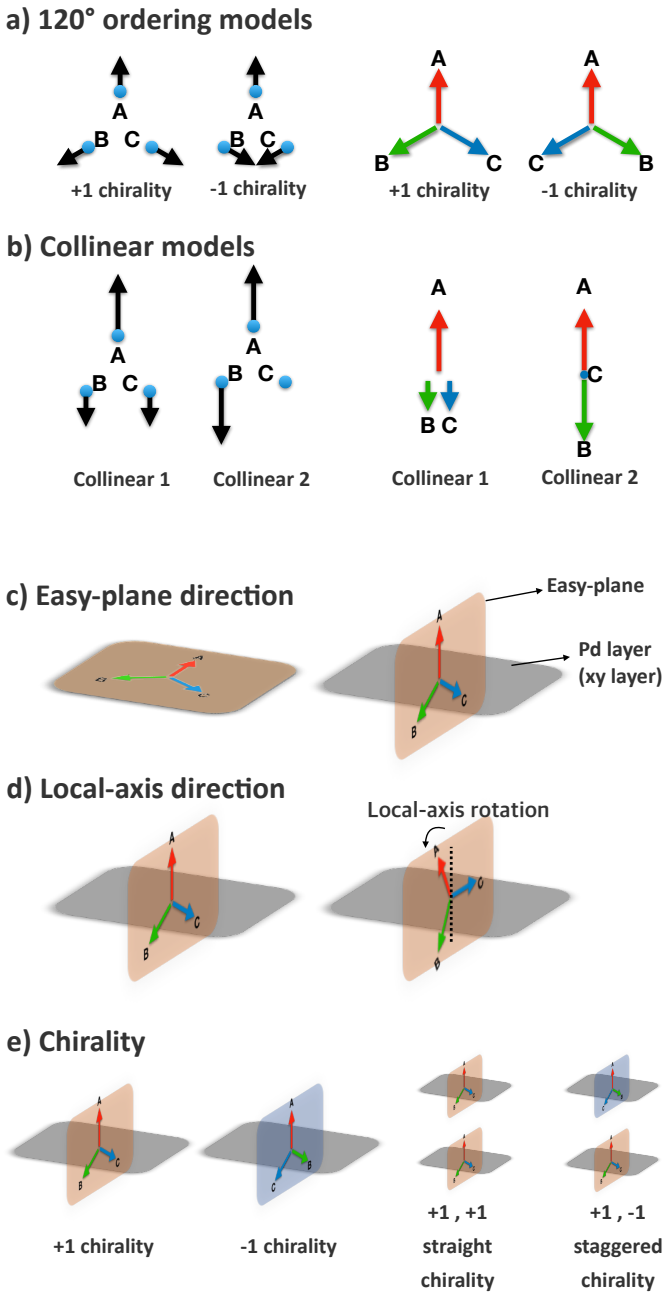

Fig. 3.3: Schematic figures of in-plane models. a) 120° models. b) Collinear models. c) Easy-plane directions. d) Local-axis directions. e) Chirality in the plane and the multi-layer structure by chiralities.

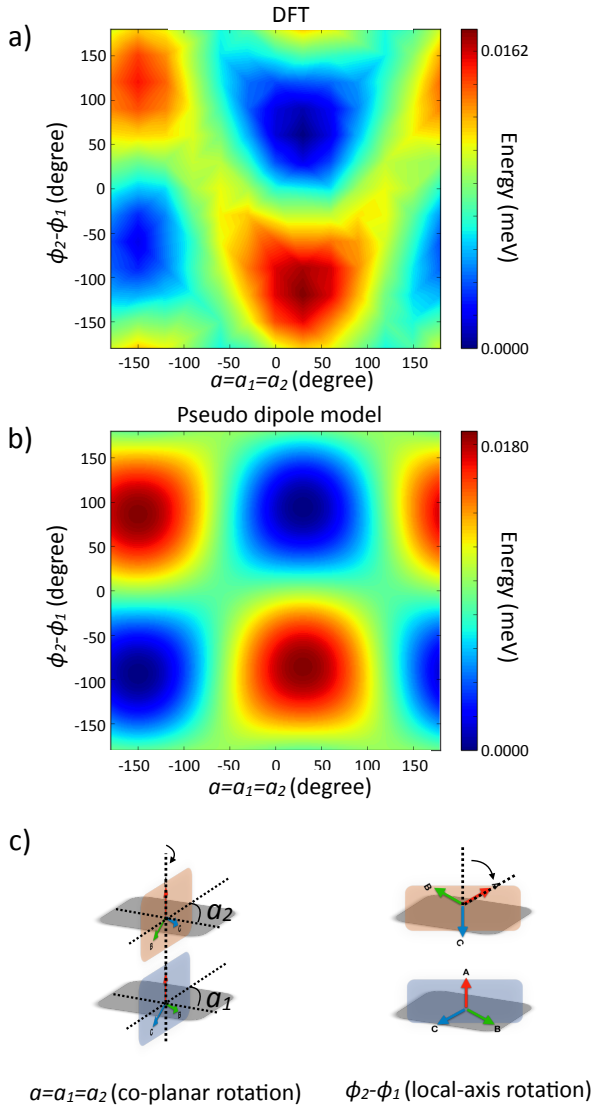

Fig. 3.4: Easy-plane ($\alpha = \alpha_1 = \alpha_2$) and local-easy-axis ($\phi = \phi_2 - \phi_1$) rotations calculated in DFT and pseudo dipole model. a) The ground state of 2-layers model in DFT calculation is $\alpha = \alpha_1 = \alpha_2 = 30^\circ$ and $\phi = \phi_2 - \phi_1 = 60^\circ$. b) Pseudo dipole model calculation. The ground state in pseudo dipole interaction is $\alpha = 30^\circ$ and $\phi = 94^\circ$. c) Schematic figures of co-planar easy-plane rotation (left) and local-easy-axis rotation (right).

$$
\begin{aligned}
S_{A_n} &= S\left[\hat{z}\cos\phi_n + \hat{e}_\alpha \sin\phi_n\right], \\
S_{B_n} &= S\left[\hat{z}\cos\left(\phi_n + \xi_n\frac{2\pi}{3}\right) + \hat{e}_\alpha \sin\left(\phi_n + \xi_n\frac{2\pi}{3}\right)\right], \\
S_{C_n} &= S\left[\hat{z}\cos\left(\phi_n - \xi_n\frac{2\pi}{3}\right) + \hat{e}_\alpha \sin\left(\phi_n - \xi_n\frac{2\pi}{3}\right)\right], \\
\hat{e}_\alpha &= \hat{x}\cos\alpha + \hat{y}\sin\alpha
\end{aligned}
\tag{3.1}
$$

S_{A_n}, S_{B_n} and S_{C_n} are local magnetic moments of atomic site A_n, B_n and C_n where n is the layer index. The easy-plane contains $\hat{z}$ and $\hat{e}_\alpha$ vectors, so the azimuthal angle α determines the easy-plane direction. We can change $\hat{z}$ and $\hat{e}_\alpha$ to another orthogonal set of two unit vectors so that we can define the easy-plane which does not contain the $\hat{z}$ vector (e.g. xy-plane). ϕ_n is local-axis rotation angle inside the easy-plane. ξ_n is ± 1, which represents chirality. However, the inversion of chirality can also be described by $\alpha \to \alpha + 180^\circ$. That means that the straight and staggered chirality is special cases of twist of two easy-planes ($\alpha_2 = \alpha_1 + 180^\circ$)

Table 3.1 show energies of collinear FM and AFM models, xy-easy-plane models and straight chirality models. The collinear AFM cannot be stabilized in a layer, so we use 2-layer collinear AFM which consist of two opposite FM layers. In this table, we find that the magnetic structure has three different energetic regions. Collinear and non-collinear spin ordering takes the strongest energy, approximately 27 meV / Cr atom. The Heisenberg interaction well describe this result. However, intriguing points are chirality (twisting mode of easy-planes) and co-planar easy-planes rotations. The energy from chirality is approximately 0.22 meV / Cr atom and that of co-planar easy-planes rotating is 0.017meV / Cr atom. The energy scale of these ro-

Table. 3.2: The proportion of orbitals at Fermi level. calculated in 20 × 20 × 20 k-points, with spin parameters in Figure. 3.6. As previous $PdCrO_2$ studies have expected, Half-filled Pd d_{z^2} is major Fermi surface constructing orbital (See Figure.3.6.c)), and other pd d components are bonding orbitals However there are still large proportion of $d_{x^2-y^2}$ and d_{xy} orbitals at Fermi level that might affect tight binding hopping models in Figure.3.7. 1.8% of Cr d_{z^2} orbital is small amount, but that could be a key feature of band structures of DFT and tight binding models, also z-directional spin interactions.

Pd	82.61%	Cr	4.85%	O	12.54%
Pd d_{z^2}	33.13%	Cr d_{z^2}	1.81%	O p_x	1.36%
Pd $d_{x^2y^2}$	18.22%	Cr $d_{x^2y^2}$	0.33%	O p_y	1.32%
Pd d_{xy}	18.22%	Cr d_{xy}	0.31%	O p_z	9.16%
Pd d_{xz}	0.44%	Cr d_{xz}	0.56%		
Pd d_{yz}	0.44%	Cr d_{yz}	0.60%		

tating modes is so small, compared to the strongest factor, the rotating modes rarely affect to AFM-FM tilting energy, and vice versa. The more intriguing point is that the co-planar rotation mode of easy-planes do not affect to chirality (or twisting of easy-plnaes). It indicates that twisitng mode and, co-planar easy-planes and local-axis rotating mode have separated origins.

We may consider three separated contributions with totally different energy scale to the magnetic interactions, which can be described by three separate effective spin models.

3.2.3 Effective spin models

Let us consider Heisenberg terms which can account for the energy difference between FM and AFM configurations as obtained from DFT calculations.

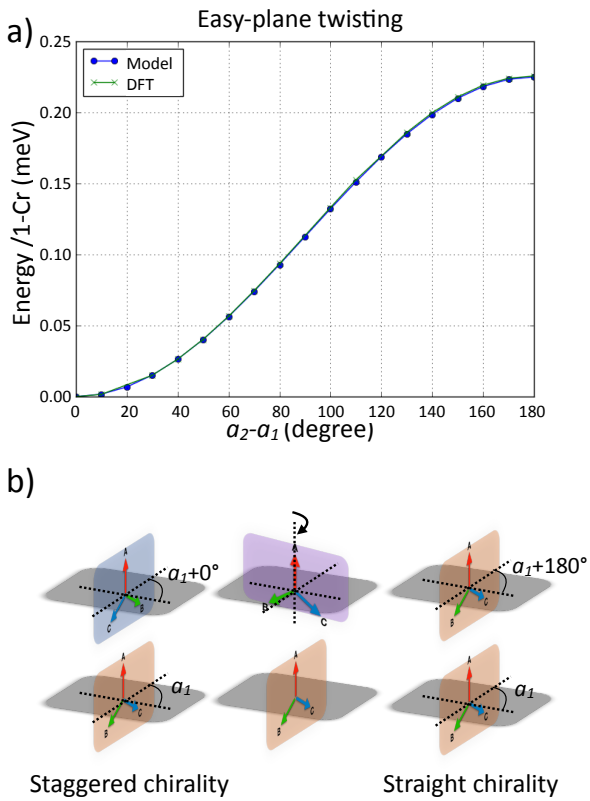

Fig. 3.5: Twisting of easy-planes and its energy. The twisting easy-planes between upper layer(α_2) and lower layer(α_1) makes a chirality reverse when 180° $\alpha_2 - \alpha_1 = 180^\circ$. a) Green line : DFT energy. blue line : Cyclic 4-spins interaction model with the parameter $J_{ring} = 0.1$meV. DFT and the model have nearly same curves. b) Schematic figures of twisted easy-planes.

$$H_1 = J_1 \sum_{\langle i,j \rangle} S_i \cdot S_j + J_2 \sum_{\langle\langle i,j \rangle\rangle} S_i \cdot S_j + J_3 \sum_{\langle\langle\langle i,j \rangle\rangle\rangle} S_i \cdot S_j + \quad \cdots \tag{3.2}$$

However, the Heisenberg terms of Eq. (2) do not contain any contribution to chirality, easy-plane and local-easy-axis directions. Also, Dzyaloshinskii-Moriya (DM) interaction is forbidden by symmetry [14, 35]. First, we show that 4-cyclic ring interactions of nearest neighbor spins can be a good effective model for chirality and twisting easy-plane mode.

There has been difficulty to make an effective model for describing easy-plane twisting or chirality. Because, previous 2-spins interaction models do not separate those twisting mode from FM tilting or co-planar easy-plane rotation and local-axis rotation. The energy from straight and staggered chirality must contain a product term of two spin rotation parameter ξ_n, also it has to be separated from ϕ_n and co-planar ($\alpha_n = \alpha_{n+1}$) rotation mode. To accomplish two conditions, we suppose a product of relative spin directions of each layers. To describe the relative spin direction, we need at least two spins in a layer. Therefore, the minimum description of our suggestion can be two spins and two spins interactions, which has total four spins. Subsequently, we assume the nearest interactions, which is the simplest form within the first assumption. Then, the selected four nearest neighbor spins form a cyclic loop. Finally, we suppose the interaction is hopping of local Cr so that we can transform local magnetic moments to spinors.

The following effective model is what we suggest

$$H_{cyclic} = J_{ring} \sum_{i}^{\substack{cyclic- \\ rings}} \left\langle S_i|S_j \right\rangle \left\langle S_j|S_k \right\rangle \left\langle S_k|S_l \right\rangle \left\langle S_l|S_i \right\rangle$$
$$|S_n\rangle = \begin{pmatrix} \cos\frac{\theta_n}{2} \\ \sin\frac{\theta_n}{2} e^{i\varphi_n} \end{pmatrix} \tag{3.3}$$

where S_i, S_j, S_k, S_l is a sequence of Cr local spins in the 1st nearest cyclic loop. Not only it has an energy scale far from Heisenberg interaction energy, it is also separated from co-planar easy-planes rotating and local-axis rotating, which are the 3rd factor in DFT calculations. We can interpret that each local spin is a hopping site, and they also construct projection matrices for spins.

Fig. 3.5 shows continuous change of easy-plane twisting ($\alpha = \alpha_2 - \alpha_1$) and its energetic behavior. When $\alpha = \alpha_2 - \alpha_1 = 180^\circ$, the chirality is reversed. The calculated energy of the model and DFT perfectly fit each other when J_{ring} = 0.1meV.

Still, there should be another interaction model to describe co-planar easy-plane rotation and local-axis. Previously, dipole interaction was suggested for a possible candidate of small energy interaction term, but they did not show an energy calculation or neutron scattering fitting for it [14]. Dipole interaction is not a good model to rescale its energy, so we set pseudo dipole interaction term as follows

$$H_{ij}^{dip} = S_i \bar{\bar{A}}_{ij} S_j \quad ,$$
$$\bar{\bar{A}}_{ij} = D_{ij} \left(3\hat{r}_{ij}\hat{r}_{ij}^{\top} - \delta_{ij} \right) \tag{3.4}$$

where $\hat{r}_{ij}$ is local easy direction between atoms at i_{th} and j_{th} sites. In Fig. 3.4, both

DFT and pseudo dipole model have $\alpha_1 = \alpha_2 = 30^\circ$ as a ground state. It is the direction contains 1st nearest inter layer connections. However DFT calculation shows minimum energy at $\phi = \phi_2 - \phi_1 = 60^\circ$, while pseudo dipole model has minimum energy at $\phi = \phi_2 - \phi_1 = 94^\circ$.

Fig 3.6 shows an electronic structure calculated in DFT with an example parameters $\alpha_1 = 31, \alpha_2 = 31, \phi_1 = 17, \phi_2 = 16, \xi_1 = 1, \xi_2 = -1$. The Fermi surface is nearly hexagonal shape on $k_z = 0$ plane, and it has very weak z-directional dispersion. Pd d electrons are the major component at the Fermi level. Pd s accounts for less than 3% of sum of Pd d electrons. Cr d_{z^2} accounts only for 1.8%. It also implies that z-directional Pd-Cr hopping is weak. One intriguing result is that there is small degeneracy breaking on the bands near the Fermi level. The degeneracy breaking is approximately 0.1 meV. To study A-site d orbital effects, we also calculated $PtCrO_2$. Fig 3.7 a) shows DFT calculation of Fermi surface of $PtCrO_2$. The Fermi surface of $PtCrO_2$ is convex (concave in 2nd zone). This result is similar to the Fermi surface of $PtCoO_2$, which is observed in ARPES [36]. The portion of Cr d electron is very small at Fermi level, but it is still essential to describe the Fermi surface.

To figure out the factor which changes Fermi surface shape and the tiny structures in electronic bands, we calculate TB models. For simplicity, we assumed that only Pd atoms have hopping sites (half filled) and Cr atoms have local magnetic moments which construct projection matrices for Pd electrons. First, the TB model is simplified to be a quasi two dimensional triangular lattice model. By assuming Pd d electrons have 1st nearest and 2nd nearest hoppings along xy-plane directions, we constructed an effective Hamiltonian

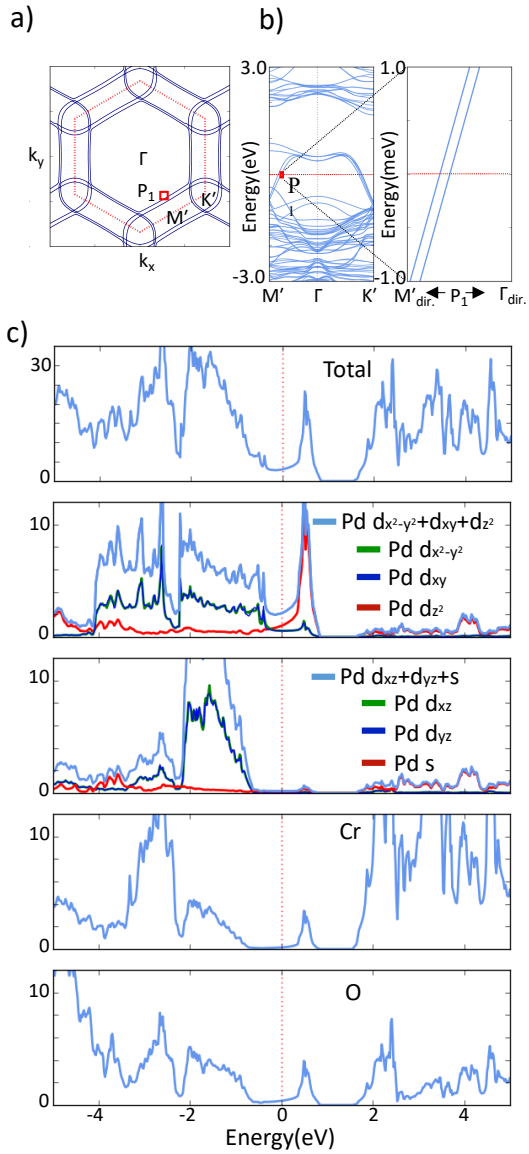

Fig. 3.6: $PdCrO_2$ electronic bands structure and PDOS. a) A Fermi surface at $k_z = 0$ plane. Since the unit cell, which we used to describe staggered chirality in DFT calculation, has inclined a_3 lattice. We used $b_2 + \frac{2}{3}b_3$ instead b_2 to illustrate $k_z = 0$ plane. Points in Figure defined as $M' = \frac{1}{2}b_1$ and $K' = \frac{2}{3}b_1 + \frac{1}{3}b_2 + \frac{2}{9}b_3$. P_1 is the 1st touching band of the line from Γ to M'. b) Band structure in $M' - \Gamma - K'$ line and P_1 zoom-in view. c) DOS and PDOS. See Table 3.2 for details of PDOS at the Fermi level.

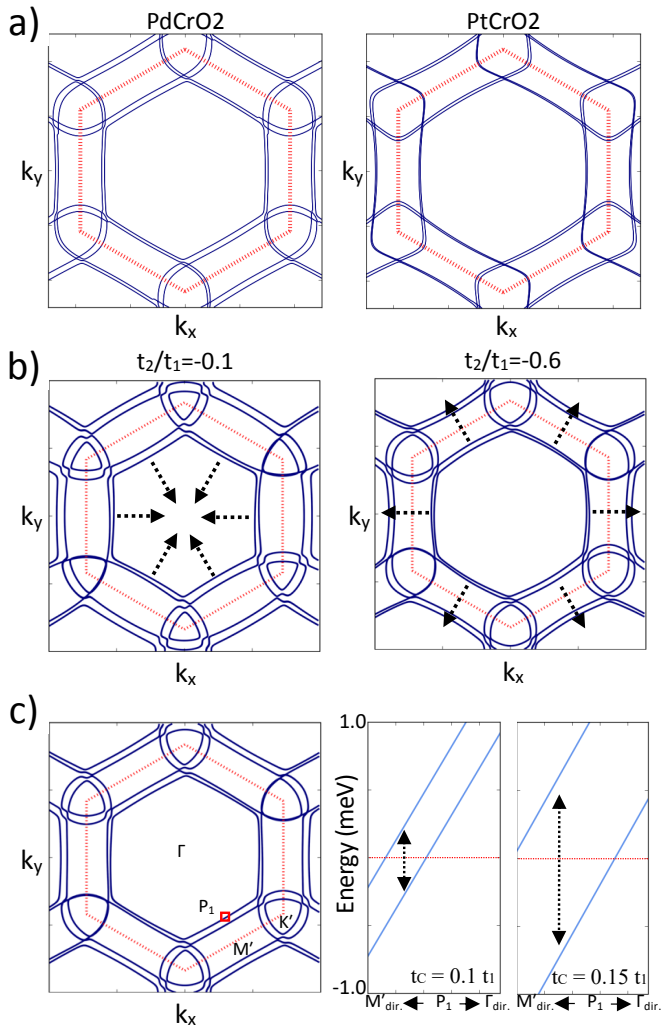

Fig. 3.7: DFT and TB calculations of Fermi surfaces at k_z=0 plane. a) DFT calculation of $PdCrO_2$ (left) and $PtCrO_2$ (right) b),c) TB calculations. b) Controlled Fermi surface shapes by second nearest direct hopping parameter t_2. $t_2 = -0.1t_1$ (left), $t_2 = -0.6t_1$ (right). c) Controlled degeneracy breaking by hopping parameter t_c. $t_c = 0.1t_1$ (middle) and $t_c = 0.15t_1$ with $t_2 = -0.35t_1$.

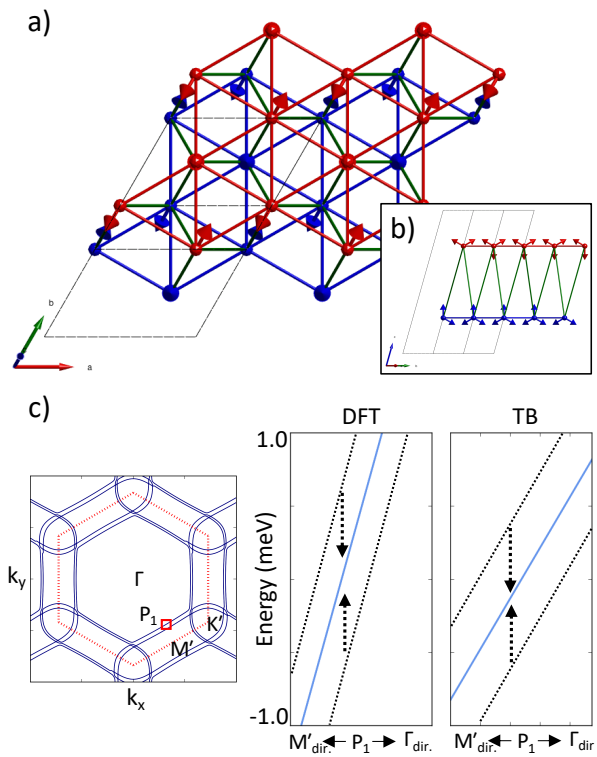

Fig. 3.8: a),b) The ground magnetic structure calculated in DFT. c) The Fermi surface of DFT calculation (left), degenerated 2 bands calculated in DFT (middle) and TB model (right).

$$H_{0,l} = t_1 \sum_{\langle i,j\rangle l\sigma} d^{\dagger}_{il\sigma} d_{jl\sigma} + t_2 \sum_{\langle\langle i,j\rangle\rangle l\sigma} d^{\dagger}_{il\sigma} d_{jl\sigma} \tag{3.5}$$

where i, j are hopping sites indices, σ is a spin index and l is a layer index. The nearest neighbor hopping t_1 and 2nd nearest neighbor hopping t_2 determine xy-planar shape of the Fermi surface. At $t_2 = -0.35t_1$, the Fermi surface is getting closer to a flat hexagonal shape. However, when t_2 changes, the shape of Fermi surface are getting closer to concave or convex shapes. When $t_2 = -0.1t_1$, a hexagonal lines become concave (convex on 2nd zone), and when $t_2 = -0.6t_1$, a hexagonal lines become convex (concave on 2nd zone). In this model, the 1st and 2nd hopping ratio of A-site of ABO_2 delaffosite is the parameter which controls Fermi surface shape.

Meanwhile, Cr atoms contribute to only small energy, but they construct z-directional connections and tiny structures on bands. We set up Pd-Cr-Pd interaction which includes inter layer hoppings.

$$\begin{aligned} H_{1,ll'} &= t_c \sum_{i,j',l,l',\sigma,\sigma',n} \langle\sigma|S_n\rangle \langle S_n|\sigma'\rangle d^{\dagger}_{il\sigma} d_{j'l'\sigma'} \\ |S_n\rangle &= \begin{pmatrix} \cos\frac{\theta_n}{2} \\ \sin\frac{\theta_n}{2} e^{i\varphi_n} \end{pmatrix} \end{aligned} \tag{3.6}$$

S_n is a non-collinear local Cr spin moment in Pd-Cr-Pd hopping path (nearest Pd-Cr hopping path). The moments on hopping path are interpreted as a projection matrix $|S_n\rangle \langle S_n|$. It creates off-diagonal term for Hamiltonian matrix, breaks degeneracy of bands. Because magnetic projection hopping terms are determined by magnetic structures, the tiny electronic structure is controlled by magnetic structures, specifi-

cally easy-plane and local-axis directions. In Fig. 3.8, it show the model describes well the degeneracy breaking in DFT. At the high symmetric magnetic structure ($\alpha = 30^\circ$,$\phi_1 = 0^\circ$ and $\phi_2 = 60^\circ$), which has the minimum energy in DFT calculation, both DFT and TB calculation show restoring of degeneracy. Therefore, although the portion of Cr is small on Fermi level, and the energy from easy-plane and local-axis rotation mode is very small, that tiny structure is very important to describe how z-directional interaction can be constructed and how the band degeneracy breaking can be controlled.

3.3 Conclusion

In this work, we studied the electronic and magnetic structures of $PdCrO_2$ with the first-principles calculations and model calculations. We used spin constraint DFT calculation method to understand the energetic behavior and the Fermi surface changes with related magnetic structures.

The ground magnetic structure is AFM staggered chirality with high symmetric easy-plane and easy-axis ($\xi_1 = +1, \xi_2 = -1, \alpha = 30^\circ, \phi_1 = 0^\circ \phi_2 = 60^\circ$). There are 3 different factors which dominate each energetic region of magnetic structures. Consequently, we suggest 3 effective spin models which contribute each energetic region separately. The strongest magnetic ordering energy comes from AFM and FM ordering, and Heisenberg interaction model easily predict their behavior. Chirality (or twisting ease-planes mode) is the 2nd factor, approximately 1/100 of the Heisenberg interaction. We suggest that the cyclic 4-spin ring interaction model effectively fit DFT result of twising easy-planes, also it is independent from the 1st and 3rd factor. The energy from co-planar ease-plane rotating and local-axis rotating mode is

the 3rd factor, they gives very small energy, approximately 1/1000 of the Heisenberg interaction. Pseudo dipole interaction model predict the same easy-plane direction with the DFT calculation, but it has ground state at $\phi = 94^\circ$. Still, the rotating mode of easy-plane and local-axis is a difficult problem in both experimental data fittings and DFT calculations. Furthermore, there could be much more complicated details on easy-plane and local-axis directions, because they can also have 6-layer, 12-layer and more multi-layer periodicity. Therefore, there should be multi-layer supercell calculations to examine further details on them.

In electronic structures, we found magnetic structure dependent Fermi surfaces. The nearly hexagonal shape of Fermi surface have a weak z-directional connection. It also have tiny degeneracy breaking, which is approximately 0.1meV. Pd d electron is the major component of it, while Cr d electrons take only small portion. However, magnetic moments of Cr atoms are very important to explain electronic structure of this system. By setting up the 1st nearest and 2nd nearest hopping TB model, we found that shape of Fermi surface is primarily controlled by A-site atoms (Pd or Pt). The result is consistent with experimental data and DFT calculation, it explains why Pt-delafossite materials have concave hexagonal shape of Fermi surfaces. Meanwhile, Cr local magnetic moments can be a bridge between Pd inter layers. Besides, they can be interpreted as perturbative spin projection terms. The Pd-Cr-Pd magnetic hopping model describes how the tiny degeneracy breaking can be constructed in the DFT calculation. Magnetic-structure-controlled degeneracy breaking might be correlated to AHE, since it changes very small energy gap between occupied band and unoccupied band [37]. Therefore, specific easy-plane, local-axis structures and their responses to external field can be the key to understand AHE in $PdCrO_2$ and related delafossite magnetic systems.

Chapter 4

Spinel Ir_2O_4

From a magnetic frustration and related novel properties, pyrochlore system has attracted the enormous interest of condensed matter society. Local tetrahedron structure of 4-spins make various kinds of magnetic multipoles, then they give intriguing physical properties. Spin ice and spin glass [38–43] systems are two intriguing examples related to 2-in-2-out structure. Quantum-order-by-disorder is originated from local-xy (m_E) structure. There are also numerous possibility of topological phase transitions which are related to magnetic phases. Pyrochlore iridates $R_2Ir_2O_7$ [44] is a notable example. Topological phases, Weyl semi metal and U(1) quantum spin liquid are predicted in it.

However, there has not been sufficient studies on a spinel $A_xB_2O_4$ pyrochlore system. Since the angle between two corner sharing tetrahedrons and B-O-B bonding angles are different from 227 pyrochlore system, the physical property of spinel is also different from 227 materials. Recently, a study reported that effective $J_{eff,1/2}$ electrons in spinel structure can have novel magnetic structures because of its large next nearest neighbor(NNN) interactions [50]. It is because the B-O-B nearest neighbor (NN) connection in spinel has 90° bonding angle. If $J_{eff,1/2}$ orbitals have a 90° angle in superexchange path with p orbitals, effective superexchange Hamiltonian becomes zero, since the π bonding of d orbital and p orbital restrict possible bonding paths. Unfortunately, there are very few experimental data of spinel Ir_2O_4. In a decade ago, H. Kuriyama et al.[45] was synthesized an iridium spinel oxide sample

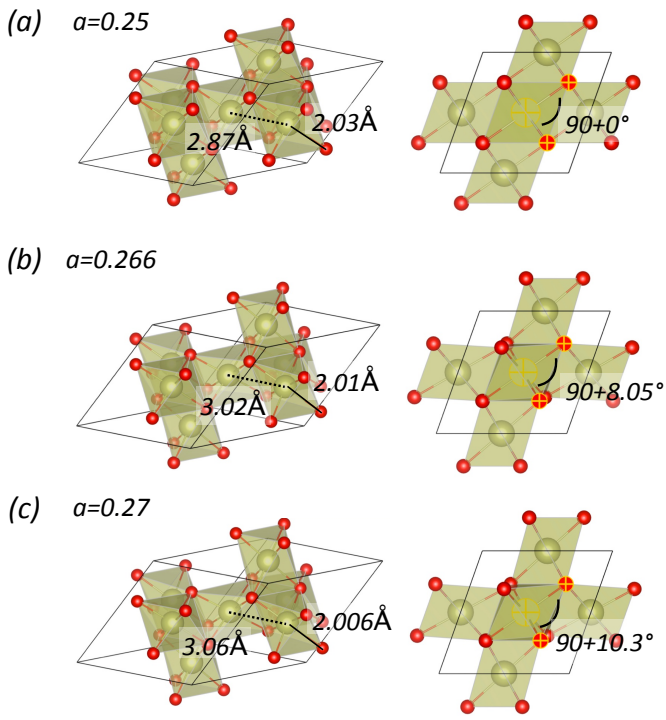

Fig. 4.9: Structure of iridium spinel oxide. (a) Ir_2O_4 with perfect oxygen octahedron. (b) A structure at the phase transition point of *m*-order parameters. (c) The ground state structure. (α, α, α) is a Wyckoff position of oxygen.

for the first time, by *Li*-deintercalation method with an epitaxially grown $Li_xIr_2O_4$. They report that Ir atoms possibly have effective $J_{eff,1/2}$ orbitals by spin-orbit Mott interactions. However, the magnetic properties and oxygen position in the crystal is still unknown. Theoretically, an investigation on the magnetic ground state of Ir_2O_4 was published a few month ago [42]. They predicts 2-in-2-out like spin-ice system, based on nearly perfect 90° angle of Ir-O-Ir bondings. However, they did not report bonding angle effects and magnetic phase transition by external pressure.

Therefore, in this paper, we study the magnetic structures in iridium spinel oxide Ir_2O_4 and its pressure-controlled phase transitions for the first time. We use the density functional theory to establish the magnetic ground state and show that the phase transition can occur by external pressure. The magnetic phase transition might be originated from effective spin interaction of NN and NNN. We also show that the ratio between NN and NNN interaction energy can be controlled by Ir-O-Ir angles.

4.1 Method

OpenMX package [46–48] is used for main DFT calculations, and VASP is used for cross-checks. To obtain energy of each magnetic phase, we carry out spin constraint methods. Both Zeeman constraint and penalty function constraint method [30] are used. When Zeeman constraint is applied to local magnets, each local magnetic moment can be stretched by Zeeman field. In that cases, the stretched magnetic moment tends to increase DFT energy, it leads to additional error of magnetic phase energy. Therefore, along with the Zeeman constraint method, we also use a correction for magnetic-moment-stertching error by constructing a spin-stretching function. Because the constraint method in DFT does not guarantee all spin-excited states to be perfect with *m*-order parameter states, we ignore mixed *m*-order parameter states for

accuracy. Local-spin density functional of Cerpeley Alder (LSDA-CA) [2] along with RMM-DIISH [31] mixing scheme is used which gives better performance for convergence of non-collinear magnetic structures. LDA+U method [32] with coulomb interaction energy 1.5 eV $< U <$ 2.7 eV on Ir d-orbitals is used to get insulator states and to obtain a U-dependent magnetic phase diagram. We use 4-Iridium unit cell, which is the smallest cell to describe m-order parameters. Results are robust from K-points $5\times5\times5$ to $10\times10\times10$, and the minimum scf-criterion 0.05 meV / Ir-atom is used.

4.2 backgrounds

By the crystal field of surrounding oxygen ions, Ir $5d$-orbtials are spiltted into t_{2g} and e_g orbitals. Also, strong spin-orbit coupling of Ir splits t_{2g} orbitals into $J_{eff,3/2}$ and $J_{eff,1/2}$ orbitals. Since Ir^{4+} contains 5 electrons, $J_{eff,3/2}$ is fully filled and $J_{eff,1/2}$ orbitals become half-filled. $J_{eff,1/2}$ orbitals consist the near-Fermi level bands. Strong electron correlations of Ir split $J_{eff,1/2}$ bands, creating the magnetic moment at each site. Therefore, here we consider that each Ir ion carries effective spin-1/2.

The magnetic structure in pyrochlore lattice with spin-1/2 can be understood with its symmetry and the magnetic order (m-order) parameter concept [49]. In the pyrochlore lattice, the magnetic structures contains total 12 (4 sites $\times$ 3 dimension) degrees of freedom. Those 12 degrees of freedom are classified into 5 different kinds of magnetic structures, all-in-all-out (AIAO) (m_{A_2}), local-xy (m_E), ferromagnetic ($m_{T_{1A}}$), T_1-octupole ($m_{T_{1B}}$), and Palmer-Chalker m_{T_2}. These are called m-order parameter or cluster magnetic multipoles. Because $m_{T_{1A}}$ and $m_{T_{1B}}$ are frequently mixed to become splayed ferromagnet (SFM, $m_{T_{1A'}}$), the predicted magnetic phases are all-in-all-out, local-xy, Palmer-Chalker and SFM in Fig. 4.10. Note that the well-

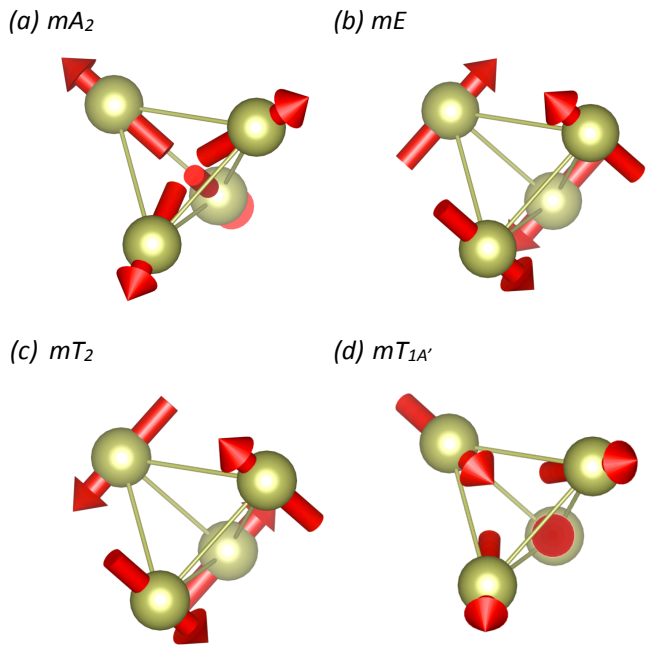

Fig. 4.10: Schematic figures of m-order parameters. Since the $m_{T_{1A'}}$ phase is only stabilized for mixed state of $m_{T_{1A}}$ and $m_{T_{1B}}$, there are only 4 possible m-order parameters.

known spin ice ordering or 2-in-2-out phase requires single-ion-anisotropy (SIA). Thus, although the 2-in-2-out phase can be described using m-order parameters, the perfect 2-in-2-out phase without SIA is unlikely to emerge.

4.3 Results

4.3.1 Magnetic structures

Without external pressure, the oxygen octahedron which surrounds an iridium atom is distorted from regular octahedron. Hence, we define the angle of O-Ir-O nearest bonding, as $90\pm x^\circ$ to describe distortion of the octahedron. The calculated distortion angle x is about 10° at the zero pressure. However, the distortion angle decreases by applying external pressure, and the change in the energy of each magnetic structures follows.

The ground state at zero pressure is m_E. the energy difference between $m_E(\Psi_2)$ and $m_E(\Psi_3)$ is very small, so within the SCF-criterion which we used in OpenMX, $m_E(\Psi_2)$ and $m_E(\Psi_3)$ cannot be distinguished. This result is consistent with the nearest neighbor (NN) spin interaction model and its m-order parameter theory [49]. $m_{T_{1A'}}$ phase is the 2nd lowest energy phase at zero pressure. When the distortion angle (or internal coordinate α) decreases, $m_{T_{1A'}}$ has the ground energy. The phase transition point and its pressure are around $x = 8^\circ$ and 4.5 Gpa. The phase transition point slightly decrease by lowering Hubbard interaction U. m_{T_2} phase is the 3rd lowest energy phase and m_{A_2} phase is the 4th lowest energy phase for all distortion angles and pressures. Each magnetic phase energies have nearly quadratic dispersion. The energy dispersion converges at $x = 3^\circ$, makes minimum magnetic energy difference. This point is around the pressure of 10 Gpa. All DFT results found to be consistent

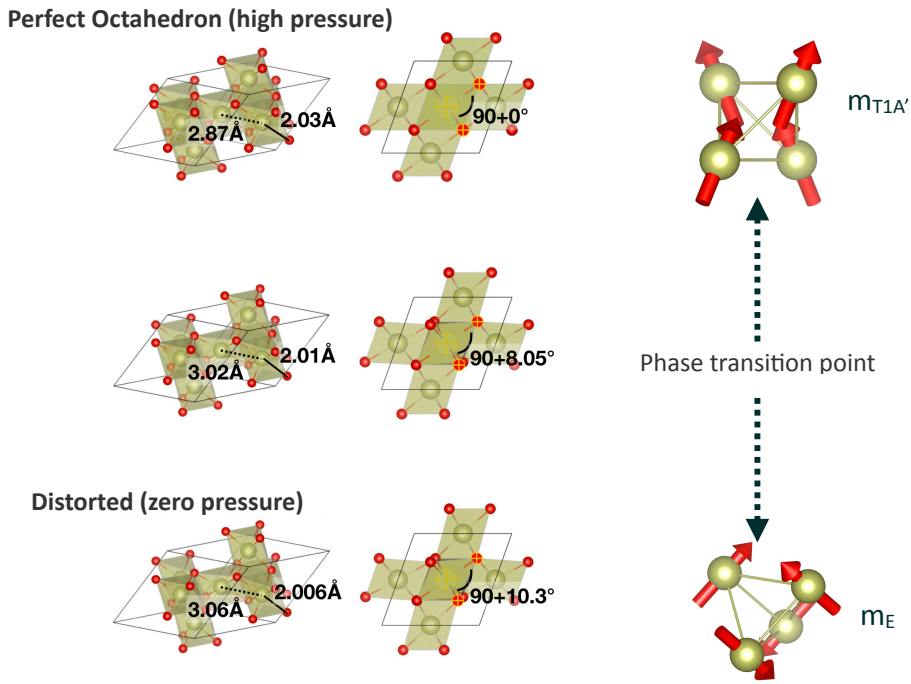

Fig. 4.11: Schematic figures of pressure-controlled Ir_2O_4 magnetic phases. DFT calculations predict mE ground phase and its phase transition to $mT_{1A'}$ by applying external pressure. The oxygen position and its distortion angle of octahedron are expected to be the parameter which control magnetic phases.

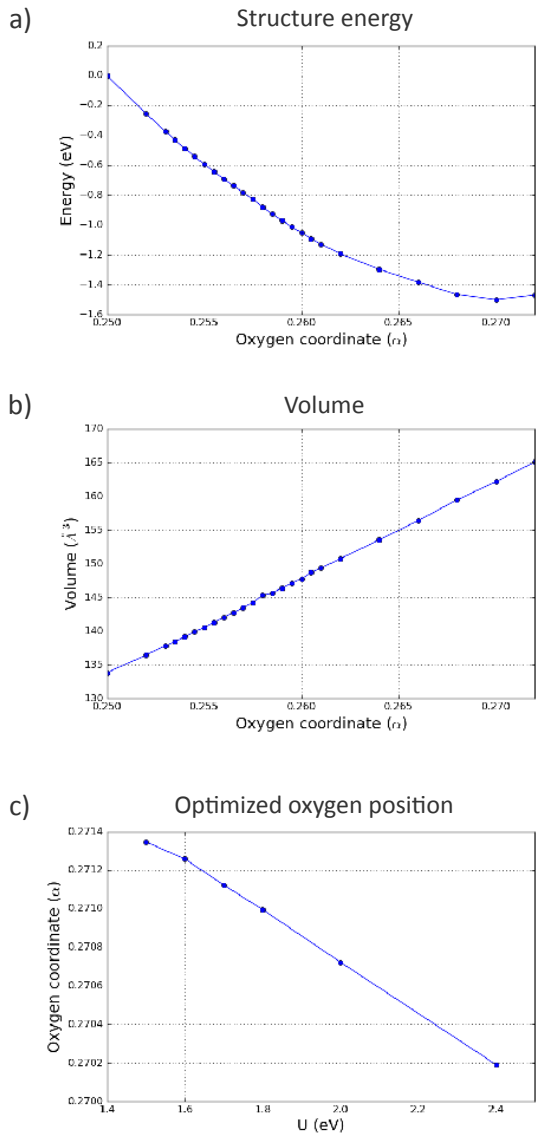

Fig. 4.12: (a),(b) and (c) Internal coordinate of oxygen and its distortion angle, bonding length and pressure. OpenMX package was used with U=2.4 eV on iridiums. (a) Distortion angle of oxygen octahedrons (O-Ir-O angle). (b) Calculated bonding length of Ir-Ir (blue) and Ir-O (red) after relaxations with fixed oxygen position (α). (c) Calculated pressure with fixed α (or unit cell volume). (d) Coulomb interaction U and ground oxygen position in DFT calculation. By increasing U, internal coordinate α (oxygen atom position at ground state) decreases.

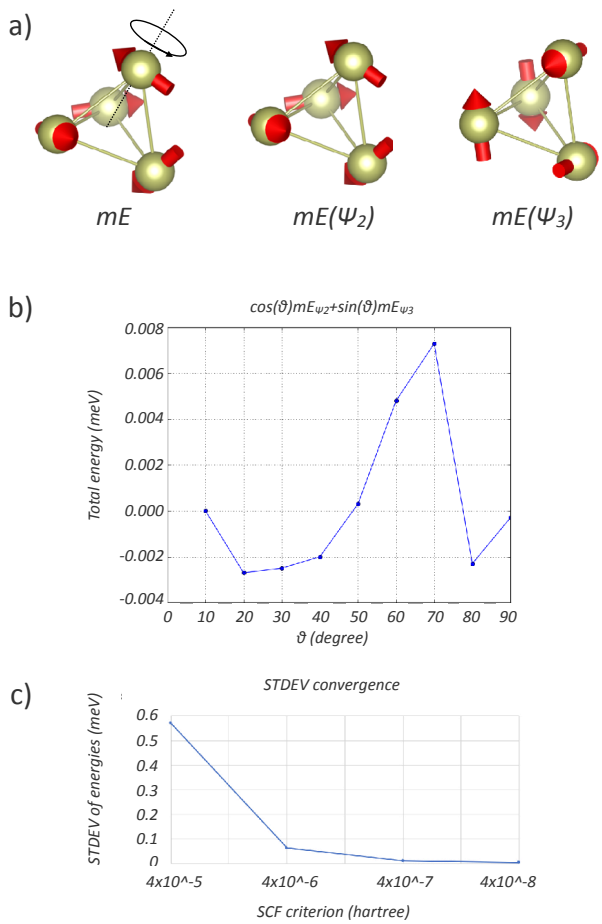

Fig. 4.13: a) Schematic figures of *mE* phase and its 2 substructures. b) A energy calculation of *mE* phases by changing their mixing of Ψ_2 and Ψ_3. The energetic error of mixed states primarily comes from mixed mT_1A' phases. c) Standard deviation of *mE* phase energies. By reducing SCF criterion, we found that the energy difference between two substructures converges to zero.

within $1.5eV < U < 2.7eV$, there is only small shift of phase transition point, distortion angle at the ground state and small change of energy scale. 2-in-2-out phases are found to be unstable in the DFT calculation. Despite the Zeeman and penalty function constraints, initial 2-in-2-out local magnets always converged to vicinal splayed-ferro phases. The unstability of 2-in-2-out phase indicates that the system does not have strong SIA interaction, compared to NN interactions. The small shift of phase transition point by changing U indicates that the phase transition must be correlated with both U and NN bondings, so we also calculate effective spin models and Hubbard models.

4.3.2 Nearest spin interactions in spinel

From the calculated energy ordering of m-order parameters, we can estimate few simple spin interaction models. The first term is the nearest spin interactions. Generally, the nearest spin interaction in pyrochlore system can be represented with four interaction terms. However, the degree of freedom in calculated m-order parameters is only 3, so there can be over-fitting problems if we try to fit DFT data into simple pyrochlore interaction model. Fortunately, spinel has its special symmetries, we can reduce the degree of freedom of the nearest spin interaction model.

Spinel structure has a C_2 rotation symmetry in the 1st nearest neighbor bonding of Ir-Ir, also a mirror symmetry [50]. From this two symmetries, the 1st nearest spin interaction can be symmetrized by Ω, the parameter controls the strength of Dzyaloshinskii-Moriya(DM) interaction. Also, the 2nd nearest bonding of Ir-Ir has its C_2 symmetry rotation axis again, it gives parameters θ and ϕ, which denote strength

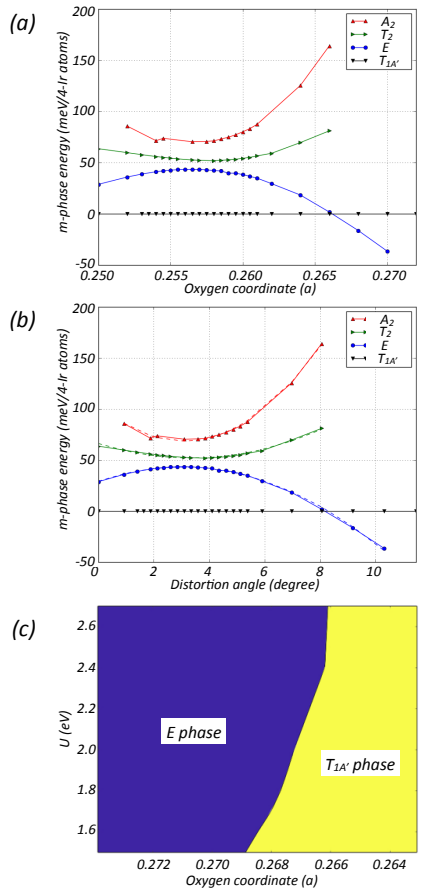

Fig. 4.14: (a) and (b) m-order parameter energy in DFT calculation (U=2.4 eV). (a) x axis for oxygen coordinate α. (b) x axis for distortion angle. m-order parameter energies are fitted with quadratic function (dotted line). The point where energy difference becomes the minimum is correspond to the non-injective region of pressure calculation. (c) A phase diagram of the DFT calculation.

and direction. The tight-binding form of the symmetrized model is

$$H = H_0 + H_U, \tag{4.1}$$

where

$$\begin{aligned} H_0 =& \sum_{\langle ij \rangle} c_i^\dagger t_{nn} (\cos\Omega + i \sin\Omega \, \vec{d}_{ij} \cdot \vec{\sigma}) c_j \quad + \sum_{\langle\langle ij \rangle\rangle} c_i^\dagger t_{nnn} (\cos\theta + i \sin\theta \, \vec{d}'_{ij}(\phi) \cdot \vec{\sigma}) c'_j, \\ H_U =& U \sum_i n_{i\uparrow} n_{i\downarrow}, \end{aligned} \tag{4.2}$$

i, j denotes the lattice sites, $t_{nn}(t_{nnn})$ is the (next-)nearest-neighbor hopping amplitude, U is the Hubbard repulsion strength. By assuming $U \gg t$, the tight-binding model can be transformed to an effective spin model as follows

$$\begin{aligned} H_{ij} \to \frac{t_{ij}^2 + d_{ij}^2}{U} (& (\cos 2\theta) \, (S_i \cdot S_j) + (\sin 2\theta) \, \hat{d}_{ij} \cdot (S_i \times S_j) \\ & + (1 - \cos 2\theta) \left(S_i \cdot \hat{d}_{ij}\right) \left(S_j \cdot \hat{d}_{ij}\right)) \end{aligned} \tag{4.3}$$

For the 2nd nearest terms, $\hat{d}$ contains a direction parameter ϕ, but the 1st nearest term does not have it. As a result, the 1st and 2nd nearest spin interaction model in spinel structure is

$$H = \sum_{\langle ij \rangle} J_{ij}^{\alpha\beta} \, (\Omega) \, S_i^\alpha S_j^\beta + \sum_{\langle\langle ij \rangle\rangle} J'^{\alpha\beta}_{ij} \, (\phi, \theta) \, S_i^\alpha S_j^\beta, \tag{4.4}$$

Each term, respectively, has degree-of-freedom two (scale and Ω) and three (scale, θ and ϕ).

By assuming the 2nd nearest interaction as a perturbative term, we can reduce the degree-of-freedom of spin interaction model to two. Then, the calculated m-order

parameter energies can be fitted into the nearest spin interaction model. Figure 4.15 shows how the ground state mE and other states can be interpreted by the 1st nearest spin interaction model. when $\Omega \simeq 1.23 + \varepsilon$, energies of m-order parameters in the NN spin model are consistent with the DFT result at zero pressure. However, this model never gives $m_{T_{1A'}}$ ground state, so the magnetic phase transition in DFT calculation cannot be represented by 1st nearest interaction. One possible candidate for the magnetic phase transition and $m_{T_{1A'}}$ ground state is the 2nd nearest term.

4.3.3 Pressure-controlled superexchange hoppings

In this section, we argue how an effective Hamiltonian of $J_{eff,1/2}$ orbitals in spinel can be controlled by bonding angles. We use Slater-Koster parametrization method and its special application of $p-d$ π bondings, which is introduced by Pesin and Balents [51]. The idea is that hopping terms between Ir t_{2g} and O p orbitals are restricted by its symmetry. Only π bonding is allowed in this case, and some of them become zero depending on their hopping directions. Following matrices are matrix representations of possible hopping path between p_x, p_y, p_z and d_{yz}, d_{zx}, d_{xy}.

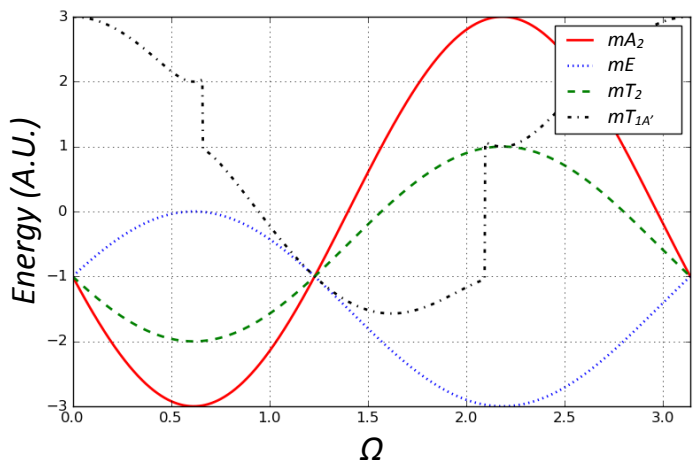

Fig. 4.15: m-order parameter energies of nearest spin interaction model. The spin interaction model is parameterized by Ω with the symmetry of spinel. An energy sequence mE, $mT_{1A'}$, mT_2 and mA_2 can be found in $\Omega \simeq 1.23 + \varepsilon$, but there is not a region which $mT_{1A'}$ is ground state. Therefore, nearest neighbor spin interaction model in spinel well describe the DFT calculation result in ground, while there should be additional interaction energy terms to describe the magnetic phase transition.

$$\tau_x = \begin{pmatrix} 0 & 0 & 0 \\ 0 & 0 & 1 \\ 0 & 1 & 0 \end{pmatrix},$$
$$\tau_y = \begin{pmatrix} 0 & 0 & 1 \\ 0 & 0 & 0 \\ 1 & 0 & 0 \end{pmatrix},$$
$$\tau_z = \begin{pmatrix} 0 & 1 & 0 \\ 1 & 0 & 0 \\ 0 & 0 & 0 \end{pmatrix}. \tag{4.5}$$

Since the 1st nearest superexchange hopping path is 90° in perfect octahedron spinel, only one type of π bonding become non-zero for one path. Also, one pair of nearest Ir-Ir bonding have 2 superexchange paths. We can describe it using τ matrix notation as follows

$$t^{ii'} = t\tau_{ii'}(I^i)(I^{i'})\tau_{i'i}. \tag{4.6}$$

I is identity matrix and $\tau_{ii'}$ is a proper selection of τ_x, τ_y, τ_z components. Two paths for one ii' pair must be summed. Because Ir have $J_{eff,1/2}$ electrons, a unitary transforms for $J_{eff,1/2}$ orbitals must be added on $t^{ii'}$. The unitary transform for $J_{eff,1/2}$ is

$$\left|\frac{1}{2},+\frac{1}{2}\right\rangle = \frac{1}{\sqrt{3}}(yz,\downarrow + ixz,\downarrow + xy,\uparrow), \tag{4.7}$$
$$\left|\frac{1}{2},-\frac{1}{2}\right\rangle = \frac{1}{\sqrt{3}}(yz,\uparrow - ixz,\uparrow - xy,\downarrow). \tag{4.8}$$

Then, the effective Hamiltonian of $J_{eff,1/2}$ become zero

$$H_{eff} = \begin{pmatrix} 0 & 0 \\ 0 & 0 \end{pmatrix} \tag{4.9}$$

When oxygen octahedron has perfect shape, the first nearest neighbor superexchange is suppressed by its symmetry.

However, when the oxygen octahedron is distorted, there must be a correction on effective hopping matrix $t^{ii'}$. Each hopping path has its rotation transformation respectively. The corrected hopping can be described as

$$\begin{aligned} R(\alpha) &= r(\alpha) \otimes D(\alpha), \\ t^{ii'} &= t\,\tau_{ii'} \left(R^{i}(\alpha)\right)^{\dagger} R^{i'}(\alpha)\,\tau_{i'i}. \end{aligned} \tag{4.10}$$

α is Wyckoff position of oxygen atoms, $r(\alpha)$ is spatial rotation and $D(\alpha)$ is spinor rotation. We assume that octahedron distortion is small enough to keep original t_{2g} orbital shapes and their energy level. We also ignore effects of bonding length and corresponding crystal fields. Then, the effective Hamiltonian of α-dependent $J_{eff,1/2}$ hopping becomes

$$\begin{aligned} H_{eff,1/2} &= \begin{pmatrix} h_{11} & 0 \\ 0 & h_{22} \end{pmatrix}, \\ h_{11} &= h_{22} \end{aligned} \tag{4.11}$$

The diagonal term h_{11} of effective Hamiltonian is nearly linear to α when the distortion of octahedron is small. When Coulomb interaction U is strong enough, effective spin interactions can be approximated as $J \sim t^2/U$. Therefore, a spin interaction ratio between the 1st nearest and 2nd nearest (J_{NN}/J_{NNN}) can be controlled by oxygen position α. Since DFT results show an α reducing effect by external pressure, it means that the 2nd nearest spin interaction terms can be enhanced by pressure.

We show one possible example of NN+NNN spin interaction model in figure 4.16. This toy model is the NN+NNN+U Hubbard model, which is non-approximated form of NN+NNN spin interaction model. To describe non-collinear spin with the TB form, we define a local magnetic moment at atom i as follows

$$\vec{m}_i = \frac{1}{2}\sum_i c^{\dagger}_{i\alpha}\vec{\sigma}_{\alpha\beta}c_{i\beta}. \tag{4.12}$$

We use a high symmetric parameter set to plot the example in figure 4.16, while there are many other (Ω, θ, ϕ) candidates which can have $m_E - m_{T_{1A'}}$ phase transition. In the model, the ratio between t_{nnn} and t_{nn} controls the phase transition. Comparing the phase diagram with DFT phase diagram, we show the model and DFT calculations are consistent with the α dependent effective Hamiltonian scheme.

4.4 Discussion

So far, we investigate the ground state of a spinel Ir_2O_4 and its pressure-induced magnetic phase transitions. The DFT calculation shows that octahedron of oxygen atoms is distorted, the Wyckoff position is $\alpha \sim 0.27$. The ground magnetic phase is m_E and two substructure $m_E(\Psi_2)$ and $m_E(\Psi_3)$ have same energy. This result imply that spinel Ir_2O_4 can be a strong candidate for quantum-order-by-disorder material

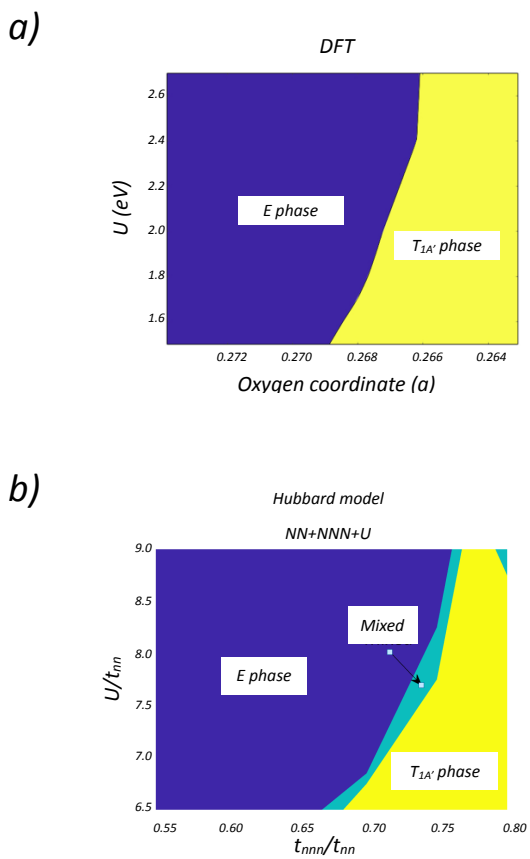

Fig. 4.16: A comparison of magnetic ground phases. a) DFT calculations. b) Hubbard model calculations. We used a numerical iterative Hubbard model calculation method to avoid approximation errors in effective spin models. The model is spinel symmetrized NN+NNN+U and we used a paramter set (Ω, θ, ϕ) =$(1.33, \pi/2, \pi/3)$

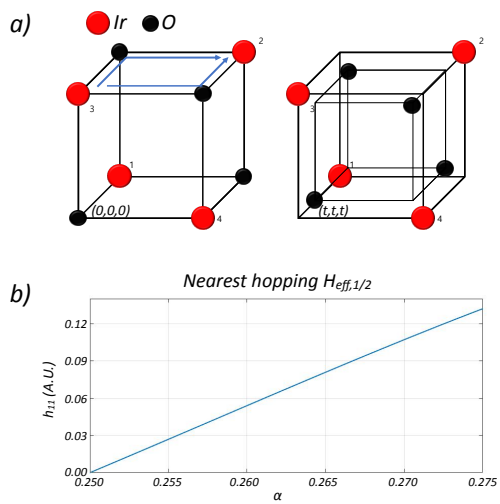

Fig. 4.17: a) Nearest superexchange hopping path in perfectcell (left) and distorted cell (right). t = 4(α-0.25). Ir-O-Ir hopping angle in distorted cell is not 90° , it restores nearest superexchanges. b) Calculation of nearest superexchange hopping in simple $d-p-d$ hopping TB model. α is a coordinate for Wyckoff positions of oxygen atoms.

[52, 53]. When unit cell is crammed by pressure, oxygen octahedron is restored to perfect octahedron, and there is a magnetic phase transition point that $m_{T_{1A'}}$ phase has the ground energy. The NN spin interaction models in pyrochlore structures generally have degree-of-freedom of four, but it can be reduced to two by the symmetry of spinel. Magnetic phases and their energies at zero pressure can be explained by the spinel-symmetrized NN spin interaction model. However, NN model does not explain a phase transition to $m_{T_{1A'}}$, so we need extra terms. The 2nd nearest neighbor (NNN) interaction is an important factor, because 90° angle of NN indirect hopping path suppresses NN superexchange of $J_{eff,1/2}$ orbitals. We calculated effective Hamiltonian for $J_{eff,1/2}$ electrons, using Slater-Koster parametrization method. The distorted oxygen position (α) controls the NN superexchange interaction, so spin interaction ratio between NN and NNN (J_{NN}/J_{NNN}) can be controlled by pressure.

The result of our DFT calculation shows that the external pressure can induce magnetic phase transition from m_E-phase to $m_{T_{1A'}}$-phase. By comparing Slater-Koster parametrization and the DFT result, we discuss how the oxygen octahedron distortion affects to magnetic phases with its superexchange enhancing effect. We also found that the Hubbard model calculation with special paramter set has the same magnetic phase transition with the DFT calculation. Since the Hubbard model is just a NN+NNN+U toy model with a special symmetry, further research for other symmetric parameter sets is required.

We suggest that the pressure-controlled magnetic phase transition in spinel can be a new platform of topological phase transitions. For many times, a correlation between magnetic phase transition and topological phase transition has been studied in 227 pyrochlore structure. However, there is very few study on spinel structure despite its possibility of novel properties. Especially, $m_{T_{1A'}}$ phase is known to be correlated to

field-induced topological semimetals [54]. Therefore, we expect that our Ir_2O_4 study can be a connection to advanced studies of spinel pyrochlore systems.

Chapter 5

Summary

We have investigated magnetic structures in novel magnetic frustration systems. For theoretical investigation, we used DFT calculation method with OpenMX and VASP packages. The magnetic structure calculation in DFT needs high precision, so we focused our efforts to error-reducing process of converged spins and SCF-criterions. To achieve this goal, technically, there should be specific combinations of mixing scheme, grids and exchange-correlation functional. The optimized combination of DFT calculation parameters allow us to get high precision results (e.g. we use the SCF-criterion energy approximately 1 μeV / atom). We successfully calculated tiny magnetic structures which are not clear in experimental data.

For ten years, there have been a numerous efforts to investigate delafossite $PdCrO_2$. Thanks for those efforts, we now understand the basic magnetic structure and related physical properties. However, details on the magnetic structures and related anomalous Hall effect is still unrevealed. We hope that our DFT calculations and Cr spin interaction models can illuminate the secret of spin chirality, easy-plane and related anomalous Hall effect.

Meanwhile, spinel Ir_2O_4 is a new area of the pyrochlore frustration system. There are many experimental and theoretical study in pyrochlore 227 structures. The 227 pyrochlore materials have attracted attention of the magnetic material physics society with their possibility of novel magnetic and topological properties. However, the study in pyrochlore spinel has just begun. There are very few experimental data

and theoretical suggestion in this field. We hope that our result of m_E phase and $m_{T_{1A'}}$ phase transition in Ir_2O_4 can open a new possiblity of novel pyrochlore magnetic material study.

Bibliography

[1] P. Hohenberg and W. Kohn, Physical review **136**, B864 (1964).

[2] D. M. Ceperley and B. Alder, Physical Review Letters **45**, 566 (1980).

[3] J. P. Perdew, K. Burke, and M. Ernzerhof, Physical review letters **77**, 3865 (1996).

[4] J. C. Phillips, Physical Review **112**, 685 (1958).

[5] T. Ozaki, Physical Review B **67**, 155108 (2003).

[6] C.-C. Lee, Y. Yamada-Takamura, and T. Ozaki, Journal of Physics: Condensed Matter **25**, 345501 (2013).

[7] S. Dudarev, G. Botton, S. Savrasov, C. Humphreys, and A. Sutton, Physical Review B **57**, 1505 (1998).

[8] H. Takatsu, H. Yoshizawa, S. Yonezawa, and Y. Maeno, Physical Review B **79**, 104424 (2009).

[9] H. Takatsu, S. Yonezawa, S. Fujimoto, and Y. Maeno, Physical review letters **105**, 137201 (2010).

[10] J. M. Ok, Y. Jo, K. Kim, T. Shishidou, E. Choi, H.-J. Noh, T. Oguchi, B. Min, and J. S. Kim, Physical review letters **111**, 176405 (2013).

[11] H. Takatsu, G. Nénert, H. Kadowaki, H. Yoshizawa, M. Enderle, S. Yonezawa, Y. Maeno, J. Kim, N. Tsuji, M. Takata, *et al.*, Physical Review B **89**, 104408 (2014).

[12] H.-J. Noh, J. Jeong, B. Chang, D. Jeong, H. S. Moon, E.-J. Cho, J. M. Ok, J. S. Kim, K. Kim, B. Min, *et al.*, Scientific reports **4**, 3680 (2014).

[13] D. Billington, D. Ernsting, T. E. Millichamp, C. Lester, S. B. Dugdale, D. Kersh, J. A. Duffy, S. R. Giblin, J. W. Taylor, P. Manuel, *et al.*, Scientific reports **5**, 12428 (2015).

[14] M. D. Le, S. Jeon, A. I. Kolesnikov, D. Voneshen, A. Gibbs, J. S. Kim, J. Jeong, H.-J. Noh, C. Park, J. Yu, *et al.*, Physical Review B **98**, 024429 (2018).

[15] F. Lechermann, Physical Review Materials **2**, 085004 (2018).

[16] J. A. Sobota, K. Kim, H. Takatsu, M. Hashimoto, S.-K. Mo, Z. Hussain, T. Oguchi, T. Shishidou, Y. Maeno, B. I. Min, *et al.*, Physical Review B **88**, 125109 (2013).

[17] S. Ghannadzadeh, S. Licciardello, S. Arsenijević, P. Robinson, H. Takatsu, M. Katsnelson, and N. Hussey, Nature communications **8**, 15001 (2017).

[18] H. Kadowaki, H. Takei, and K. Motoya, Journal of Physics: Condensed Matter **7**, 6869 (1995).

[19] M.-T. Suzuki, T. Koretsune, M. Ochi, and R. Arita, Physical Review B **95**, 094406 (2017).

[20] S. Nakatsuji, N. Kiyohara, and T. Higo, Nature **527**, 212 (2015).

[21] S. Toth and B. Lake, Journal of Physics: Condensed Matter **27**, 166002 (2015).

[22] A. P. Mackenzie, Reports on Progress in Physics **80**, 032501 (2017).

[23] K. Kim, H. C. Choi, and B. Min, Physical Review B **80**, 035116 (2009).

[24] H.-J. Noh, J. Jeong, J. Jeong, E.-J. Cho, S. B. Kim, K. Kim, B. Min, and H.-D. Kim, Physical review letters **102**, 256404 (2009).

[25] C. W. Hicks, A. S. Gibbs, L. Zhao, P. Kushwaha, H. Borrmann, A. P. Mackenzie, H. Takatsu, S. Yonezawa, Y. Maeno, and E. A. Yelland, Physical Review B **92**, 014425 (2015).

[26] H. Takatsu, S. Yonezawa, C. Michioka, K. Yoshimura, and Y. Maeno, in *Journal of Physics: Conference Series*, Vol. 200 (IOP Publishing, 2010) p. 012198.

[27] V. Sunko, F. Mazzola, S. Kitamura, S. Khim, P. Kushwaha, O. Clark, M. Watson, I. Markovic, D. Biswas, L. Pourovskii, *et al.*, arXiv preprint arXiv:1809.08972 (2018).

[28] T. Ozaki and H. Kino, Physical Review B **69**, 195113 (2004).

[29] M. J. Han, T. Ozaki, and J. Yu, Physical Review B **73**, 045110 (2006).

[30] P. Kurz, F. Förster, L. Nordström, G. Bihlmayer, and S. Blügel, Physical Review B **69**, 024415 (2004).

[31] G. Kresse and J. Furthmüller, Physical review B **54**, 11169 (1996).

[32] A. Liechtenstein, V. Anisimov, and J. Zaanen, Physical Review B **52**, R5467 (1995).

[33] S. Tóth, B. Wehinger, K. Rolfs, T. Birol, U. Stuhr, H. Takatsu, K. Kimura, T. Kimura, H. M. Rønnow, and C. Rüegg, Nature communications **7**, 13547 (2016).

[34] A. Jain, S. P. Ong, G. Hautier, W. Chen, W. D. Richards, S. Dacek, S. Cholia, D. Gunter, D. Skinner, G. Ceder, *et al.*, Apl Materials **1**, 011002 (2013).

[35] T. Moriya, Physical Review **120**, 91 (1960).

[36] P. Kushwaha, V. Sunko, P. J. Moll, L. Bawden, J. M. Riley, N. Nandi, H. Rosner, M. P. Schmidt, F. Arnold, E. Hassinger, *et al.*, Science advances **1**, e1500692 (2015).

[37] X. Wang, J. R. Yates, I. Souza, and D. Vanderbilt, Physical Review B **74**, 195118 (2006).

[38] P. A. Lee, Science **321**, 1306 (2008).

[39] L. Balents, Nature **464**, 199 (2010).

[40] M. Hermele, M. P. Fisher, and L. Balents, Physical Review B **69**, 064404 (2004).

[41] H. R. Molavian, M. J. Gingras, and B. Canals, Physical review letters **98**, 157204 (2007).

[42] S. Onoda and F. Ishii, Physical review letters **122**, 067201 (2019).

[43] C. Booth, J. Gardner, G. Kwei, R. Heffner, F. Bridges, and M. Subramanian, Physical Review B **62**, R755 (2000).

[44] X. Wan, A. M. Turner, A. Vishwanath, and S. Y. Savrasov, Physical Review B **83**, 205101 (2011).

[45] H. Kuriyama, J. Matsuno, S. Niitaka, M. Uchida, D. Hashizume, A. Nakao, K. Sugimoto, H. Ohsumi, M. Takata, and H. Takagi, Applied Physics Letters **96**, 182103 (2010).

[46] T. Ozaki, Physical Review B **67**, 155108 (2003).

[47] T. Ozaki and H. Kino, Physical Review B **69**, 195113 (2004).

[48] M. J. Han, T. Ozaki, and J. Yu, Physical Review B **73**, 045110 (2006).

[49] H. Yan, O. Benton, L. Jaubert, and N. Shannon, Physical Review B **95**, 094422 (2017).

[50] G. Sim and S. Lee, Physical Review B **98**, 014423 (2018).

[51] D. Pesin and L. Balents, Nature Physics **6**, 376 (2010).

[52] L. Savary, K. A. Ross, B. D. Gaulin, J. P. Ruff, and L. Balents, Physical review letters **109**, 167201 (2012).

[53] K. A. Ross, L. Savary, B. D. Gaulin, and L. Balents, Physical Review X **1**, 021002 (2011).

[54] T. Oh, H. Ishizuka, and B.-J. Yang, Physical Review B **98**, 144409 (2018).

초 록

Delafossite $PdCrO_2$와 spinel Ir_2O_4 의 자기 구조를 연구하였다. Delafossite $PdCrO_2$는 Pd층과 CrO_2층이 교차하는 형태의 삼각 anti-ferromagnetism(AFM) 층상 구조 물질이다. 전도성인 Pd층은 *xy* 방향의 높은 전도성에 기여하고, 한편 Cr 원자의 국소 자기 모멘트들은 anomalous Hall 효과에 기여한다. 중성자 회절 실험과 각분해 광전자 분광법 실험을 통해, $PdCrO_2$의 자기 구조가 삼각 120° AFM 정렬을 *xy* 평면으로, 6층 구조를 *z* 방향으로 이룬다는 것이 예측된다. 그러나, scalar chirality, 교차 chirality, 비틀어진 easy-plane들, easy-plane의 방향 과 같은 구체적인 구조들이 분명하게 이해되고 있지는 않다. 한편 spinel Ir_2O_4는 pyrochlore $J_{eff,1/2}$ 시스템중 하나이다. Ir_2O_4의 산소의 위치와 자기적 특성은 보고되지 않았다. 또한 spinel $J_{eff,1/2}$ 시스템의 이론적 배경도 pyrochlore 227 시스템에 비해 충분하지 않아, spinel Ir_2O_4를 연구하기 위한 정보가 적은 상태이다. 이번 연구에서, 우리는 밀도 범함수 이론(DFT)에 근거하여 두 물질의 자기구조와 전자구조를 계산하였다. $PdCrO_2$의 바닥 상태는 높은 대칭구조의 평면 교차 chirality 구조이고, Ir_2O_4는 *mE* (국소-*xy*) 상태이다. 우리는 또한, 스핀 상호작용 모델과 관련하여, 각각의 자기 구조들의 원인도 제시한다.

주요어 : 자성체,밀도 범함수 이론,Ir_2O_4,$PdCrO_2$

학번 : 2013-20370